STUDY OF MICROSTRUCTURE EVOLUTION IN F/M STEEL T91 BY IN-SITU SYNCHROTRON WIDE-ANGLE X-RAYS SCATTERING

BY

JINSHENG WANG

THESIS

Submitted in partial fulfillment of the requirements
for the degree of Master of Science in Nuclear, Plasma, and Radiological Engineering
in the Graduate College of the
University of Illinois at Urbana-Champaign, 2017

Urbana, Illinois

Master's Committee:

Professor James F. Stubbins, Chair
Assistant Professor Yang Zhang

Abstract

T91 ferritic-martensitic (F/M) steel is one of the leading candidates for high temperature structural materials in advanced nuclear power applications. *In situ* Wide-angle X-ray Scattering (WAXS) was used to investigate T91 during tensile test under 3 different temperatures: room temperature (RT), 450°C, 550°C, respectively. By fitting scattering patterns, information of diffraction peaks and their variation trends with respect to macroscopic strain were recorded for further analysis of Fe matrix, $M_{23}C_6$ and MX precipitates. Lattice strain of Fe matrix and precipitates were obtained from peaks shift in WAXS pattern during tensile test. Load partitioning effect, which is known as precipitates can bear higher load than Fe matrix, was found to be less obvious within plastic regime with the increase of temperature from RT to 550°C. Peak broadening, represented by full width at half maximum (FWHM), was carefully analyzed using modified Williamson-Hall (W-H) plots to separate strain and crystalline size effects due to their different θ dependence. It was found that dislocation density ρ in Fe matrix behaved differently within different tensile regimes: before Ultimate Tensile Strength (UTS), they all increased; after UTS, it plateaued first then increased at end for RT, remained stable for 450°C while decreased continuously for 550°C. Coherent scattering length L_{310} calculated by Scherrer Equation using Fe(310) plane behaved as below: before UTS, they all decreased; after UTS, it decreased continuously for RT, remained stable for 450°C and rose dramatically for 550°C. The variation trends of both dislocation density and coherent scattering length L_{310} were impacted by combination effect from high temperature and tensile flow stress evolution.

Scanning Electron Microscopy (SEM), Optical Micropy (OM) and Transmission Electron Microscopy (TEM) were also used to study the post-tensile samples. SEM found that at RT tensile fracture happened violently with huge cracks on necking center cross-section, while fracture happened slowly with voids and dimples on cross-section under higher temperatures. SEM Energy Dispersive Spectroscopy (EDS) mapping also found that rupture protrusions on necking center edges had higher C and N concentration than that of metallic elements. OM revealed the martensitic plates and ferrites in T91 after polishing and etching. Lastly, TEM experiment was also carried out using Focused Ion Beam (FIB) prepared specimen to characterize precipitates, dislocations and other microscale features, and to compare with the previous X-rays Diffraction

(XRD) results.

Acknowledgments

To begin with, I would like to thank my advisor, Professor Stubbins, for giving me such a valuable opportunity to join his research group, as well as offering funding support and research guide. He cares about students as much as possible for the sake of the students.

Besides, I am grateful to Professor Zhang for reviewing and revising this thesis. Moreover, I also would like to thank my colleagues, Xiang Liu, Kuan-Che Lan, Huan Yan and Hoon Lee for helping me with experiments and instructive discussions. This work would be impossible without them.

Lastly, special thanks to my parents for their love and support over the years.

Table of Contents

List of Tables . . . . . **vii**

List of Figures . . . . . **viii**

List of Abbreviations . . . . . **ix**

List of Symbols . . . . . **x**

Chapter 1 INTRODUCTION **1**
1.1 The Need of High Temperature Alloys in NPPs 1
1.2 9-12% Cr F/M Steels 2
1.3 Thesis Structure 3

Chapter 2 METHODOLOGY **4**
2.1 X-ray Diffraction 4
2.2 Samples Preparation 5
2.3 In-situ Tensile Test 6

Chapter 3 DATA PROCESSING BY PEAK FITTING **8**
3.1 Data Processing Flow 8
3.2 Peak Identification 11
3.3 Lattice Spacing and Peak Broadening Analysis 13
3.3.1 Lattice spacing and strain 13
3.3.2 Broadening fitting and correction 13
3.3.3 Broadening analysis with modified W-H plot 15
3.3.4 Scherrer equation for crystalline size 15

Chapter 4 RESULTS FROM XRD **18**
4.1 Macroscopic Stress-Strain Curve 18
4.2 Lattice Strain Evolution 19
4.3 Anisotropy Effect 22
4.4 Load Partitioning Effect 23
4.5 Dislocation Density Evolution 26
4.6 Coherent Scattering Length Evolution 30

Chapter 5 MICROSCOPY STUDY **32**
5.1 SEM Study of Fracture Surface 32
5.2 OM Study of Grains 34
5.3 TEM Study of Dislocation, Grains and Precipitates 39

Chapter 6 DISCUSSION AND COMPARISON **43**
6.1 Macroscopic Stress Strain Performance 43
6.2 Microscopic Phase Performance 44
6.3 Dislocation and Grain Comparison 45

Chapter 7 CONCLUSIONS AND FUTURE WORK 47
7.1 In-situ XRD Tensile Test Conclusions 47
7.2 Electron Microscopy Conclusions 48
7.3 Limitations And Future Work 48

Appendix A Peak Broadening Separation With Pseudo-Voigt Profile 50

References 52

List of Tables

2.1 Major chemical compositions for SA-533-B, SA-508-2, G91, G92, HT9 and T91. 5

3.1 Lattice parameters a (in Å) of α-Fe matrix, $M_{23}C_6$ and Nb(C,N) precipitates in G91 and G92 under RT. 12
3.2 Bulk diffraction selection rules for BCC and FCC. 13

4.1 YS and UTS (in MPa); macro ultimate tensile strain (ϵ_{UTS}) and macro fracture strain (ϵ_F) for 3 temperatures. 19
4.2 Lattice parameters a (in Å) of α-Fe matrix and $M_{23}C_6$ precipitates under RT, $450°C$ and $550°C$. 20
4.3 Young's moduli E and Poisson ratio ν for Fe and $M_{23}C_6$ planes in tensile and transverse directions. 23
4.4 Dislocation contrast factor C for diffraction planes in Fe-matrix. 28

List of Figures

1.1 Temperature and dose requirements for in core application parts in advanced NPPs. 2

2.1 Sample looking before and after tensile test. 6
2.2 Experiment setup of In-situ XRD tensile test 7

3.1 One quarter of the diffracted rings after visualization. 9
3.2 Visualization of one quarter of the diffracted rings after transformation. 10
3.3 Reduced Intensity vs 2*diffraction angle at 270 degrees azimuthal angle. 10
3.4 The diagram of how the lattice spacing is calculated. 11
3.5 Individual peak fitting example using pseudo-Voigt model. 12
3.6 Phase identification plot for α-Fe matrix, $M_{23}C_6$ and Nb(C,N) precipitates 12
3.7 Schematic explanation of three sources of the broadening of diffraction peaks. 14
3.8 Example of modified W-H plot to find dislocation density and crystalline size. 16
3.9 Flow chart showing data processing procedures. 17

4.1 Macroscopic stress strain curve under 3 temperatures for T91. 19
4.2 Explanation of using linear fitting intersection to find $d^i_{hkl}(0)$. 20
4.3 Lattice strain vs macrostrain for Fe matrix and $M_{23}C_6$ precipitates. 21
4.4 Comparison of engineering stress vs lattice strain for Fe-matrix. 24
4.5 Comparison of engineering stress vs lattice strain for $M_{23}C_6$. 25
4.6 Schematic diagram of stress and strain in both tensile and transverse directions. 26
4.7 Comparison of von Mises stress vs. macrostrain for Fe matrix and $M_{23}C_6$ 27
4.8 Dislocation density evolution profiles calculated from modified W-H plots 29
4.9 Coherent scattering length L_{310} calculated using Fe(310) diffraction plane and Scherrer formula. 31

5.1 SEM experiment overview of the T91 post-tensile sample. 33
5.2 SEM fracture corner showing deformation differences. 34
5.3 SEM 1000 times magnification of post-tensile samples. 35
5.4 SEM 5000 times magnification of post-tensile samples. 36
5.5 SEM EDS composition mapping from one edge area of necking center by $450°C$ sample. . . . 37
5.6 Optical Microscope 200 magnification of $550°C$ sample after grinding and etching. 38
5.7 TEM overview of the $450°C$ specimen showing martensitic lath, ferrite and precipitates. . . . 41
5.8 TEM capture of two precipitates under 30,000 magnification. 42
5.9 TEM Bright Field (BF) and Dark Field (DF) images of dislocations under 30,000 magnification. 42

6.1 UTS of G91, G92, T91 under different temperatures. 43
6.2 Final fracture strain of G91, G92, T91 under different temperatures. 44

List of Abbreviations

F/M	Ferritic/Martensitic
RT	Room Temperature (25 °C)
XRD	X-ray Diffraction
WAXS	Wide-angle X-ray Scattering
SAXS	Small-angle X-ray Scattering
BCC	Body-centered Cubic
FCC	Face-centered Cubic
FWHM	Full Width at Half Maximum
UTS	Ultimate Tensile Strength
OM	Optical Microscopy
SEM	Scanning Electron Microscopy
EDS	Energy Dispersive Spectroscopy
TEM	Transmission Electron Microscopy
FIB	Focused Ion Beam
WBDF	Weak Beam Dark Field
EBSD	Electron Backscatter Diffraction

List of Symbols

(hkl)	Millier Indices
λ	Wave Length of X-ray
θ	Diffraction Angle
ϵ	Strain
σ	Stress
T	Temperature
d	Lattice Space
I_0	Peak Center Intensity
η	Lorentzian Fraction
L	Lorentzian Component of Peak Broadening
G	Gaussian Component of Peak Broadening
F	Peak Broadening
β	Peak Broadening
E	Young's Modulus
ν	Poisson Ratio
K	$\frac{2\sin(\theta)}{\lambda}$
D	Crystalline Size
$\boldsymbol{b}$	Burger's Vector
C	Contrast Factor
M	Adjustable Factor
$\boldsymbol{g}$	diffraction vector
ρ	Dislocation Density
k	Crystalline Shape Factor
L	Grain Related Length

Chapter 1

INTRODUCTION

Structural materials selection always stands as a core issue to the research and development of new generation Nuclear Power Plants (NPPs). Different from traditional reactors, advanced reactors are featured with higher temperatures and intenser neutron irradiation, bringing along huge challenges to nuclear structural materials. In this chapter, the backgroud of the development of high temperature Fe alloy is introduced first, followed by a brief review of a class of promising alloys, 9-12%Cr F/M Fe alloys. At the end, the goals and methods of experiments in this thesis will be given.

1.1 The Need of High Temperature Alloys in NPPs

The development and prosperity of global countries are highly dependent on the availability of energy, especially clean energy given the fact of environment pollution over the past decades [1]. Nuclear energy, first appeared in 1950s, is now playing an increasingly important role to this world due to its high energy density, good economic competitiveness and low carbon emissionm, etc [2, 3]. In order to make the best use of limited Uranium, theoretically unlimited Hydrogen isotopes in sea water, and try to close nuclear fuel cycle, a large amout of research efforts have been put to design and study the advanced Generation IV (Gen.IV) and fusion reactors around the world [4]. So far, GIF (Generation IV International Forum) has posed 6 main potential reactor concepts for further R&D activities. They are molten salt reactor (MSR), sodium fast reactor (SFR), super-critical water-cooled reactor (SCWR), lead-cooled fast reactor (LFR), gas-cooled fast reactor (GFR) and very high temperature reactor (VHTR) [4].

Currently, the typical outlet temperatures for Pressurized Water Reactor (PWR) and Boiling Water Reactor (BWR) are 320 °C and 288 °C, respectively [5]. The temperatures above are way lower than that of VHTR and SMR, which could be as high as 1000 °C. In addition, from the perspective of radiation dose, the total maximum radiation dose for LFR, MSR, GFR and SFR by decommissioning could even go up to 200 dpa (displacement per atom), which is again far higher than that of current commercial reactors [6]. As

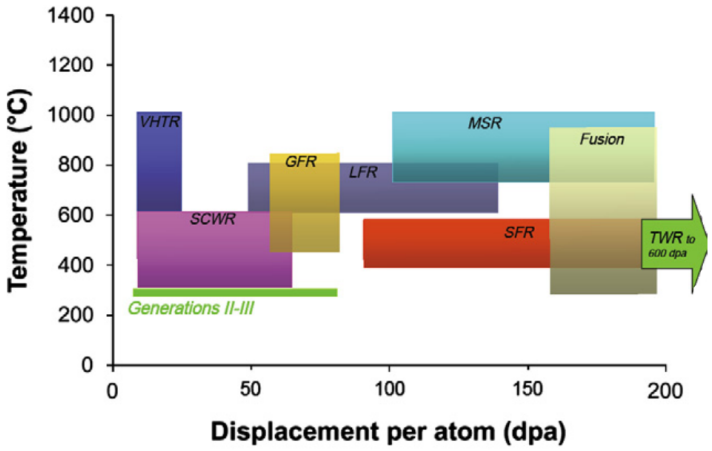

Figure 1.1: Temperature and dose requirements for in core application parts in Generation IV NPPs. Traveling wave reactor (TWR) and Fusion reactor are also included within. The figure is retrieved from Ref.[5].

mentioned above, the two major challenges for advanced NPPs are the elevated temperatures and increasing radiation dose. Previous studies have widely shown that elevated temperatures can greatly reduce UTS, mechanical strength and cause oxidation [7, 8, 9] while more radiation bombardment will degrade materials by introducing hardening, swelling and embrittlement [5, 10, 11, 12]. The figure 1.1 [5] gives a very good explanation for the high temperature and dose challenges for advanced NPPs.

1.2 9-12% Cr F/M Steels

Even before the birth of nuclear energy in 1950s, scientists had already worked on steels that can be used under extremely harsh environments for other fields such as aerospace aircrafts and traditional electricity power plants. When the concept of Nuclear Power came into existence, materials from those other fields immediately got checked to see if they can continue to work for the more challenging nuclear field.

The service environment of nuclear structural materials is usually a complex combination of several harsh factors: high temperature, aggressive coolant and high neutron flux, making the corrosion and oxidation a hard problem to be dealt with. For current Light Water Reactor (LWR), SA-533 grade B (nominally Fe-0.25C-0.24Si-0.6Ni-1.2Mn-0.5Mo) and SA-508 class 2 (nominally Fe-0.25C-0.3Cr-0.3Si-0.75Ni-0.75Mn-0.6Mo) have been widely used to construct reactor pressure vessels [13]. For advanced NPPs, Cr addition is good for corrosion resistance because the formation of dense oxide layer can prevent the further reaction of materials with the harsh environment. Other studies have also found that high Cr percentage is a good

practise to ensure the satisfactory strength of steels under high temperature such as 550 °C or even 650 °C [14]. Recent research found that 9-12% Cr F/M steels and their variations are promising to be used as one of the primary candidate materials for both out-of-core (vessels and pipes) and in-core (cladding, ducts and wrappers) applications due to their excellent corrosion and oxidation resistance performance [15, 16, 17].

When added into iron alloys, Cr can also provide little solid solution strengthening. Besides, Cr will react with Carbon to form carbide $M_{23}C_6$ and M_7C_3, where M represents Cr and C is just Carbon. These Carbides can impede the dislocation movement thus strengthen these alloys. The development of nuclear F/M steels started from the additon of Mo, Nb and V to Cr-Mo steels in 1960s, then gradually optimized by tuning the percentage of other elements such as W, N, B and Co for different purposes [14].

In this thesis study, 9% Cr F/M steel T91 (nominally Fe-9Cr-0.1C-1Mo-0.4Si-0.4Mn-VNb) was studied by in-situ XRD tensile test to investigate its macro and micro response to tensile loadings.

1.3 Thesis Structure

The structure of this thesis is arranged as below. As tradition, Chapter 1 is a short introduction to the background, and Chapter 2 talks about the details of methodology including experiment setup and sample preparation. After that, Chapter 3 will cover XRD data processing theory and process in detail followed by Chapter 4 containing the results extracted from data processing. Chapter 3 and 4 will make up the main part of this thesis. In Chapter 5, microscopy techniques were used to study the post-tensile samples, including SEM for fracture surface observation, OM for grain morphology inspection and TEM for dislocation density and grain size verification. After Chapter 5, there will be a discussion section, Chapter 6, focusing on the comparison of the results of T91 with that of G91 and G92. Finally, this thesis will conclude with Chapter 7, which will sum this thisis as well as proposing the future work.

Chapter 2

METHODOLOGY

X-ray diffraction (XRD) technique has been widely used in materials research and development (R&D) field since its birth. Diffraction patterns, combined with pre-knowledge of materials, can be used to infer the microscopic structure and macroscopic characteristics of the material, such as mechanical properties, specific heat and conductivity. This Chapter 2 will focus on the basics of XRD technique, samples preparation and the experiment procedures of tensile test with in-situ XRD.

2.1 X-ray Diffraction

X-rays (or X radiation) are composed of short-wave-length electromagnetic radiation which can penetrate into materials and interact with atoms inside. Since its birth, X-ray has been widely used in different fields, such as medical imaging, X-ray crystallography and airport security inspection. X-ray can be generated through at least two ways, one is to use X-rays tube and another is to use synchrotron radiation. For the two methods above, the intrinsic mechanisms of generating X-rays are different from each other. In a vacuum X-ray tube a heated cathode is releasing electrons which are then accelerated by high voltage to hit a metal target (usually tungsten, molybdenum or copper) to cause the release of characteristic X-rays. In this method, the released X-rays are usually of low magnitude and only have several fixed energies. Another more powerful method is to use synchrotron radiation. When charged particles are accelerated or decelerated, they will give out electromagnetic radiation, which if strong enough, will end up in the spectrum of X-rays. Modern synchrotron X-rays are generating X-rays by accelerating electrons and keeping them cycling in a high vacuum storage ring. X-rays will come out in the tangential direction of the ring, which is way better than that of X-ray tube in quality due to its high magnitude, excellent collimation, and good linear polarization.

In X-rays crystallography technique, X-rays are hitting target materials and by interaction with target atoms, the incident X-rays will be greatly diffracted into several specific directions. By recording the

diffraction patterns, the diffraction angles and diffracted intensity profiles, a crystallographer can predict the molecular or atomic configuration of the studied materials. In this study, Bragg's Law equation 2.1 was used to derive the lattice spacings of crystals in T91 steels. By recording diffraction pattern at every tensile stage, the evolution of lattice spaings can be extracted and further be used to derive other mechanical properties.

$$2d \cdot \sin(\theta) = \lambda \tag{2.1}$$

where d is d spacing between diffraction planes, θ is diffraction angle and λ is the wavelength of the incident X-ray.

In experiments of this thesis, X-rays were generated by synchrotron radiation at the Beamline 1-ID of the Advanced Photon Source (APS) in Argonne National Laboratory (ANL), IL, USA. The energy of X-ray used was 80.665 KeV, corresponding to $\lambda = 0.1536$ Å beam wavelength. The cross-section of X-ray was set to 200 μm $\times$ 200 μm.

2.2 Samples Preparation

The tensile test samples used in those experiments were cut out of T91 bulk steels, nominally composed of Fe- 9Cr-0.1C-1Mo-0.4Si-0.4Mn-0.2V-0.08Nb-0.05N, by wt.%. The shape of the samples is dog-bone, and the final geometry of these samples are around 5 $\times$ 1.2 $\times$ 0.5 in mm as shown in figure 2.1. The table 2.1 shows the major composition elements of T91 and also some other popular structural materials for comparison.

Table 2.1: Major chemical compositions for SA-533-B, SA-508-2, G91, G92, HT9 and T91 in wt.%.

Steels	C	Si	Mn	Cr	Mo	W	V	Nb	B	N	Ni
533-B	0.25	0.24	1.2		0.5						0.6
508-2	0.3	0.3	0.75		0.6						0.75
G91	0.1			9	1		0.2	0.07		0.06	
G92	0.1			9	0.5	1.8	0.2	0.08		0.06	
HT9	0.2	0.4	0.6	12	1	0.5	0.25				0.5
T91	0.1	0.4	0.4	9	1		0.2	0.08		0.05	

SA-533-B, SA-508-2 steels nearly have no Cr element, HT9 steel has 12% Cr while G91 and G92 steels have 9% Cr like T91 steel, which is the target material of this thesis. Since in-situ synchrotron XRD tensile test of G91 and G92 steels have been performed by Wang et al. in Ref. [18, 19], thus their results can be referred for comparison with that of T91 F/M steel later in this study.

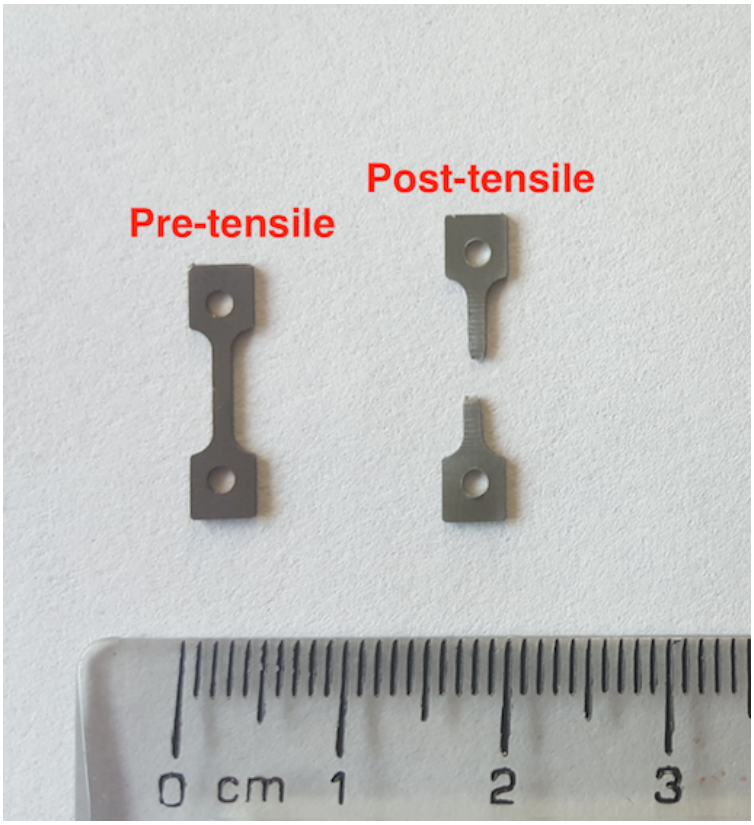

Figure 2.1: Sample looking before and after tensile test.

2.3 In-situ Tensile Test

Tensile test is a widely used, fundamental material science test method to study the mechanical properties of materials. In a typical tensile test, a sample is subject to uniaxial or biaxial controlled tension until fracture. The results from tensile tests such as ultimate tensile strength (UTS), yield strength (YS), fracture strain, Young's modulus and Poisson's ratio, can be used to judge whether certain materials are qualified for certain applications or not. Structural materials in nuclear field are crucial for the stability and reliability of NPPs given the risk of failure leading to radioactive waste leakage. As one of the promising candidates for advanced NPPs, T91 F/M steel has to go through tensile test under various conditions such as different temperatures to prove its mechanical competitiveness for further validation. In this study, 3 temperatues: RT, 450°C and 550°C were chosen to conduct tensile test to compare their performances under different tempeartures.

Synchrotron X-rays have been widely applied in various nuclear materials research field [20, 21, 22, 23] due to their high energy and brilliance compared with traditional laboratory based X-rays tubes. High

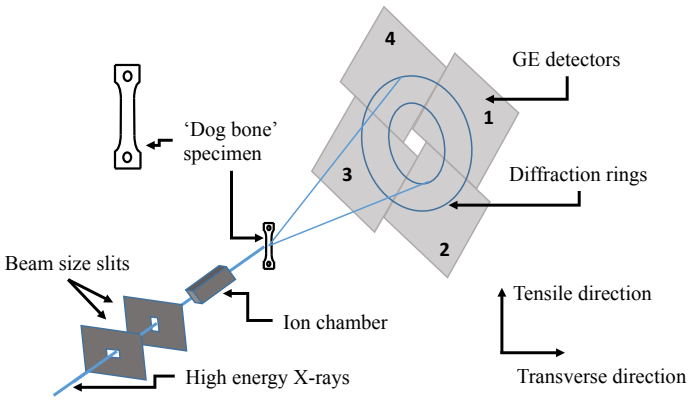

Figure 2.2: Experiment setup of In-situ XRD tensile test.

energy X-rays can penetrate alloy samples as thick as 1 mm, making it possible to conduct in-situ XRD experiments using mini size dog-bone shape samples for onsite tensile test. Wide angle X-ray scattering (WAXS) is the technique that can record the diffracted X-rays that satisfy Bragg's Law, and further to analyze the inner structure of the materials. In WAXS, diffracted peaks position information from Fe matrix and precipitates (or other particles) can be used to calculate the lattice spacings of certain (hkl) planes of certain phases by Bragg's Law. Broadening information of diffracted peaks can be analyzed to predict the dislocation density and crystalline size. Another advantage of in-situ XRD is that during tensile test X-rays keep hitting the elongated area and generating diffracted patterns at every strain stage. After fracture, the evolution of diffracted peak positions and broadenings with respect to engineering strain can be obtained and utilized to study the macro and micro response mechanisms in T91 F/M steel.

The experiment setup is shown as figure 2.2, where high, single energy X-ray was aligned and reshaped, then impinged on dog-bone shape sample center under tensile tension. At the same time, samples were heated and kept at certain temperatures. The incident X-rays went through samples, got diffracted and recorded by following detectors. Other details in terms of how data were collected and analyzed will be included in next chapter.

Chapter 3

DATA PROCESSING BY PEAK FITTING

In this chapter, how the diffracted X-rays profiles were recorded and how the collected data was processed are explained in detail. The two major characteristics of these diffracted peaks are the center positions and broadening, which correspond to information about lattice spacing, dislocation density and crystalline size. The main post-processing Matlab program used was developed by Jonathan Almer of ANL years ago.

3.1 Data Processing Flow

Just as shown in figure 2.2, after interaction with the tensile sample, the diffracted X-rays were recorded by detectors. In fact, the signal collection system is composed of 4 identical GE panels, labeled as 1, 2, 3 and 4, and each of them collected one quarter of the whole diffracted rings. Detector No.1 and No.3 were collecting the transverse direction data while No.2 and No.4 were prepared for the tensile direction. If using visualization method, one detector data can be transformed and displayed as in figure 3.1.

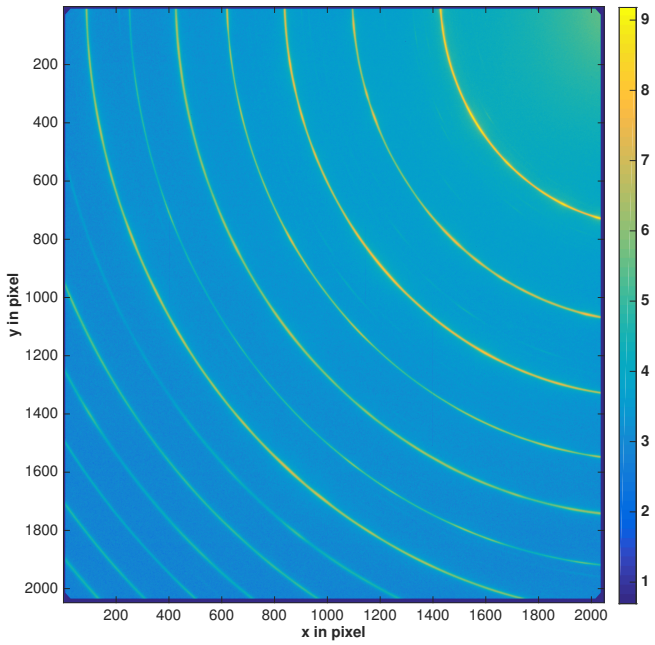

Figure 3.1: Visualization of the diffracted rings in one detector. Yellow rings had higher intensity than the blue area. One pixel size is 0.2 by 0.2 in mm.

Another way to visualize the signals collected by this detector is to transform all the data into another coordinate system. The intensity distribution can be viewed by different azimuthal angle and radius as in figure 3.2. Later it can be seen that one yellow ring is corresponding to one lattice plane of certain phase in the materials.

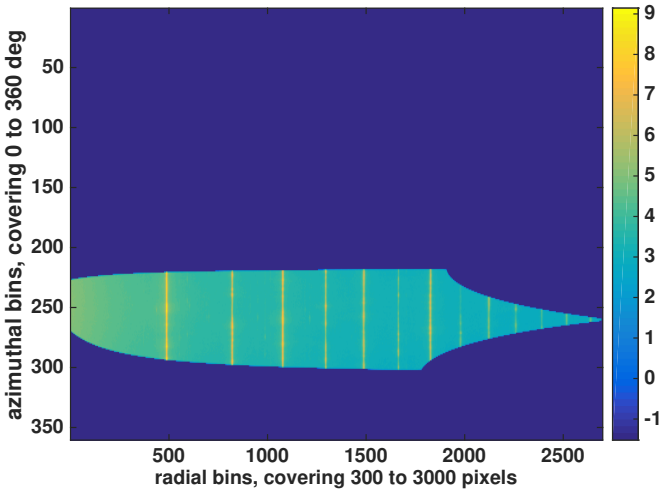

Figure 3.2: Visualization of the diffracted rings in one detector after transformation. Yellow rings had higher intensity than the blue area. One pixel size is 0.2 by 0.2 in mm. Only a few rings were fully recorded.

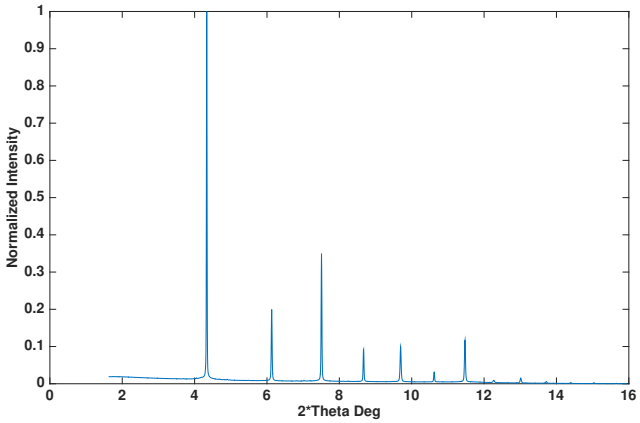

Figure 3.3: Reduced Intensity vs 2*diffraction angle at 270 degrees azimuthal angle. One peak corresponds to one plane. All peaks were normalized by the maximum intensity by Fe(110) plane.

There is one center line for each panel, 0, 90, 180, and 270 degrees, respectively. If draw a line at where azimuthal angle equals 270 degrees in figure 3.2, and calculate the diffraction angle at each radius given the constant distance from sample to panel, the diffraction profiles will be transformed into figure 3.3.

Nevertheless, figure 3.1, 3.2 and 3.3 are just preliminary results from the collected raw data. In the next section, we will move on to derive the microscopic information of the T91 samples based on the pre-processing results above.

3.2 Peak Identification

Previous results from literature have shown that there are several phases present in 9% Cr F/M steels such as α-Fe matrix, $M_{23}C_6$ and Nb(C,N) precipitates in G91 and G92 steels [18, 19]. α-Fe matrix is BCC structure while $M_{23}C_6$ and Nb(C,N) precipitates are FCC structure. Bulk material diffraction selection rules and examples for FCC and BCC atomic structures are listed in table 3.2. Figure 3.5 explained how each peak was fitted by Matlab program to find its center position and broadening values. The fitted peak center then can be transformed into lattice spacing d of certain (hkl) plane of certain phase with Bragg's equation 2.1. Other useful parameters and calculation formulas can be found in diffraction path as shown in figure 3.4.

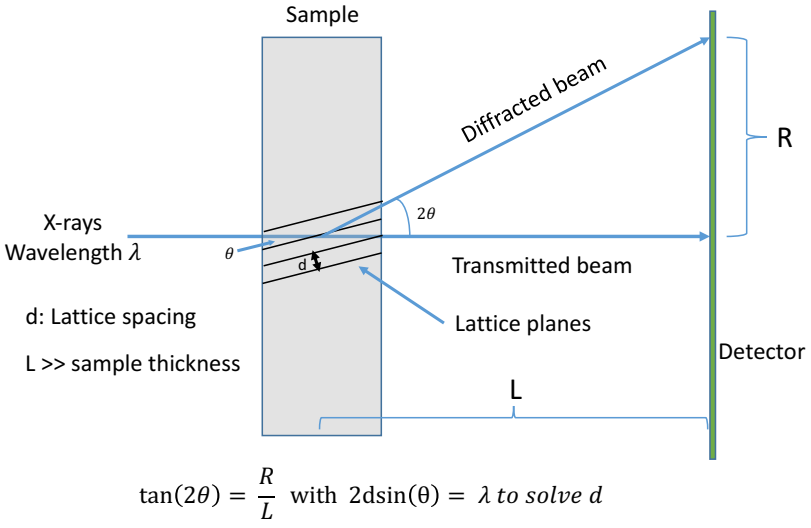

Figure 3.4: The diagram of how the lattice spacing is calculated. The length ratio between sample size, detector size and distance L, R is not for real, just for better illustration of the concept.

$$a = d\sqrt{h^2 + k^2 + l^2} \tag{3.1}$$

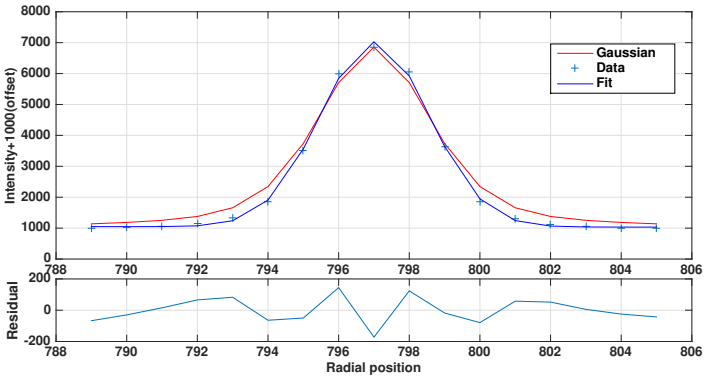

Figure 3.5: Individual peak fitting example using pseudo-Voigt model to find peak center (or position), total broadening in pixels, Gaussian fraction of total broadening for further analysis.

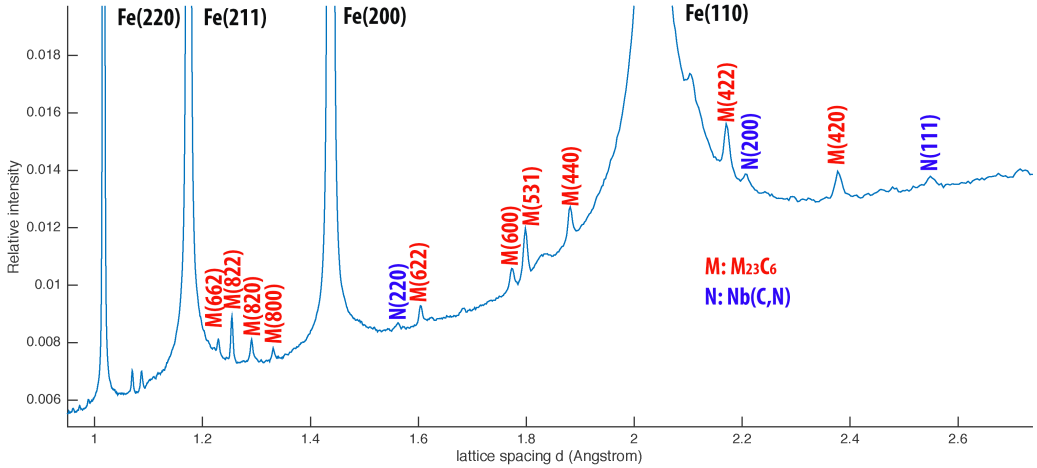

Figure 3.6: Phase identification plot for α-Fe matrix, $M_{23}C_6$ and Nb(C,N) precipitates. Transformed from figure 3.3 and labeled with phase(hkl) index.

Table 3.1: Lattice parameters a (in Å) of α-Fe matrix, $M_{23}C_6$ and Nb(C,N) precipitates in G91 and G92 under RT from Ref.[19].

steels\ phase	α-Fe	$M_{23}C_6$	Nb(C,N)
G91	2.874	10.63	4.403
G92	2.874	10.65	4.412

Table 3.2: Bulk diffraction selection rules for BCC and FCC. For BCC, allowed miller indices (hkl) satisfy h+k+l = 2n (even number) while for FCC h, k, l are all odd or even. The first 9 allowed (hkl) examples for FCC and BCC are listed as below.

BCC	(110)	(200)	(211)	(220)	(310)	(222)	(321)	(400)	(310)
FCC	(111)	(200)	(220)	(311)	(222)	(400)	(331)	(420)	(422)

Then lattice spacing values $d's$ above can be tranformed into lattice parameters $a's$ by equation 3.1 to compare with that of referrence values in Ref. [19]. Now the peak identification step is finished with figure 3.6 plotted.

3.3 Lattice Spacing and Peak Broadening Analysis

3.3.1 Lattice spacing and strain

When doing data processing work with peaks analysis, broadening, usually represented by FWHM, is another critical aspect to consider in order to fully extract all the quantitative information. In XRD tensile tests of this thesis, X-rays diffracted peaks position values have already been used to calculate the lattice spacings in the first place, which can further be used to calculate lattice strain evolution given all the spacing values available at each tensile stage by equation 3.2.

$$\epsilon^i_{hkl}(\sigma) = \frac{d^i_{hkl}(\sigma) - d^i_{hkl}(0)}{d^i_{hkl}(0)} \tag{3.2}$$

Where $d^i_{hkl}(0)$ and $d^i_{hkl}(\sigma)$ are lattice plane spacings for certain (hkl) plane in phase i before loading and after loading with applied stress σ under certain temperature, RT, 450°C or 550°C.

3.3.2 Broadening fitting and correction

In terms of total peak broadening for one peak, there are generally three factors contributing to it, instrumental broadening, strain broadening and crystalline size broadening [24] as illustrated in figure 3.7. Instrumental broadening F_{in} is sophisticated originating from experimental setup and X-ray source. However, it can be removed by standard sample correction, in which nearly self-broadening-free CeO2 or LaB6 is used to get the instrumental broadening profiles for later deduction from real samples profiles. For both standard sample peaks and true sample peaks, pseudo-Voigt, a simplified Voigt function, was used to fit

them as represented in equation 3.3.

$$V_p(2\theta) = I_0 \cdot (\eta \cdot L(2\theta) + (1-\eta) \cdot G(2\theta)) \tag{3.3}$$

Where I_0 is peak center intensity, η is Lorentzian profile fraction, $L(2\theta)$ and $G(2\theta)$ are Lorentzian and Gaussian components, repectively.

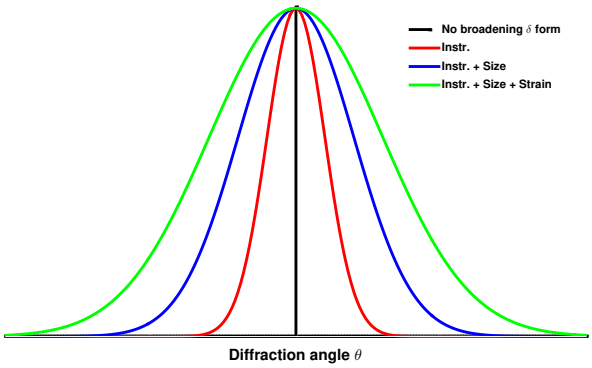

Figure 3.7: Schematic explanation of the three sources of diffraction peaks broadening. If there is no broadening, the peak would be a δ function like the central dark line. More sources of broadening would make the peak broader as shown by red, blue, green curves. In the figure, 'Instr.' stands for instrumental broadening while 'Size' and 'Strain' represent size, strain broadening, respectively. The broadening to intensity ratio in the figure is not for real, but to give a general concept.

After separation of broadening using mothods in Appendix A, Gaussian and Lorentzian part of intrumental (or standard sample) broadening, F_{in}^G and F_{in}^L should be removed from Gaussian and Lorentzian part of true samples F_{sa}^G and F_{sa}^L, respectively using equation 3.5 and 3.4 unless η is approaching either 0 or 1 like in Ref. [25, 26], which would be much easier. If η is very close to 0, meaning the dominant part is Gaussian, then equation 3.5 would already be a good approximation if treating all broadening as Gaussian part. On the countrary, if η is too close to 1, meaning Lorentzian part is dominant, then equation 3.4 would be enough by treating all broadening as Lorentzian part.

$$F_{tr}^L = F_{sa}^L - F_{in}^L \tag{3.4}$$

$$F_{tr}^{G\,2} = F_{sa}^{G\,2} - F_{in}^{G\,2} \tag{3.5}$$

Where superscript L and G means Lorentzian and Gaussian components; subscript sa, in and tr, means sample value, instrumental value and true value, respectively. After getting true broadening for both types, pseudo-Voigt method should be used to combine them back together by the way inverse to their previous

separation, which will be explained in detail in Appendix A.

3.3.3 Broadening analysis with modified W-H plot

After instrumental broadening correction, generally there exists at least two ways of finding the dislocation density and crystalline size information based on true broadening values. The first method is to use modified Williamson-Hall plot to split strain and size effects apart by taking the advantage of their different angle dependence as shown in equation 3.6.

$$\Delta K = \frac{0.9}{D_v} + (\frac{\pi M^2 b^2}{2})^{\frac{1}{2}} \rho^{\frac{1}{2}} (KC^{\frac{1}{2}}) + O(K^2 C) \tag{3.6}$$

Where ΔK is related to peak broadening by $\Delta K = 2cos(\theta)\Delta\theta/\lambda$ (here θ is diffraction angle and λ is the wavelength of incident X-ray) and $2\Delta\theta$ is exactly the FWHM of diffraction peaks in radian unit. The first right hand side term of equation 3.6 is contributed by limited crystalline size effect, where D_v is the weight averaged crystalline size, sometimes referred to as coherent scattering volume size. The second term arises from dislocation density, where $K = 2sin(\theta)/\lambda = 1/d = g_{hkl}$ (insert Bragg's law $2dsin(\theta) = \lambda$, d is d spacing of diffraction planes, g_{hkl} is the corresponding diffraction vector length), b is the length of Burger's vector (b = 0.248 nm for BCC Fe), M is an adjustable factor which was set to 1 for simplicity. ρ is dislcation density and C is contrast factor will be explained later. Other negligible broadening sources can be included in the third term, which will not be considered later on. Modified W-H plot method will do linear fitting of ΔK vs. $KC^{\frac{1}{2}}$ (or $gC^{\frac{1}{2}}$) using data from different (hkl) planes for Fe matrix. Naturally, the fitting slop is proportional to square root of dislocation density ρ while the y-intercept is 0.9 times the inverse of weight averaged crystalline size. One fitting example is shown as in figure 3.8.

3.3.4 Scherrer equation for crystalline size

Another method of using the true broadening information to find the dislocation density and crystallinse size is to use approximation. Previous studies [27] have shown that Gaussian part of broadening is highly related to straining broadening (or dislocation) while Lorentzian part is mostly from size broadening. With this approximation, there is no need to recombine the splited Gaussian part and Lorentzian part coming from equation 3.5 and 3.4 previously. Scherrer formula, shown as equation 3.7 is a good supplement of W-H plot since W-H's results are not satisfying to determine crystalline size due to the negative intercept in figure

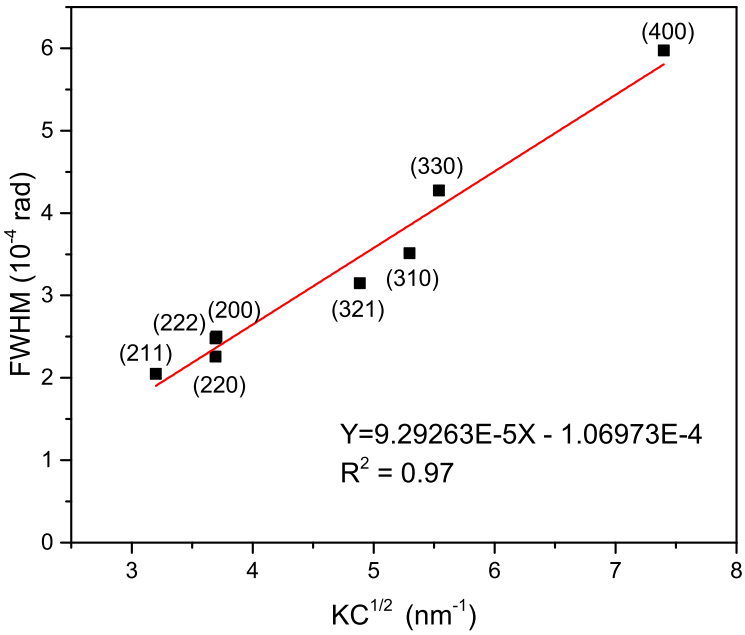

Figure 3.8: Example of modified W-H plot to find dislocation density and crystalline size. This fit plot uses 8 Fe planes from RT sample at 0 strain. This plot has a good linear fitting with 0.97 R-square but with negative intercept, which suggests possibly over-correction of instrumental broadening.

3.8. Scherrer equation will give us some insight into the crystalline size or coherent scattering length (this term is used more later in this thesis) variation trend to better understand the mechanism of materials' response in tensile tests.

$$L_{hkl} = \frac{K\lambda}{\beta^L cos(\theta)} \tag{3.7}$$

Where K is crystalline shape factor set as 1 here (sometimes set as 0.9), λ is the X-ray wavelength, θ is diffraction angle and β^L is the Lorentzian component of FWHM of peaks, calculated from equations 3.4. Scherrer equation calculation here used single profile assumption, attributing Gaussian component solely to strain broadening and Lorentzian component solely to size broadening [27].

Each of the two methods introduced above has its own advantages and disadvantages, thus in this thesis they will be combined to cover the shortcomings of each other to give the best results out of the XRD data. Later in Chapter 5, electron microscopy work, especially SEM and TEM techniques will be used to study the grain size and dislocation density information, and compare with the results from XRD peak broadening analysis above.

To sum up this chapter, especially the data processing procedures above, a flow chart as figure 3.9 is

drawn to give a straightforward explanation. For each tensile stage, do peaks fitting to obtain center positions and broadening values, and futher leverage modified W-H plot and Scherrer equation to get dislocation and crystalline size information. At the end, these values of each tensile stage were combined together to inspect their variation trends versus engineering strain.

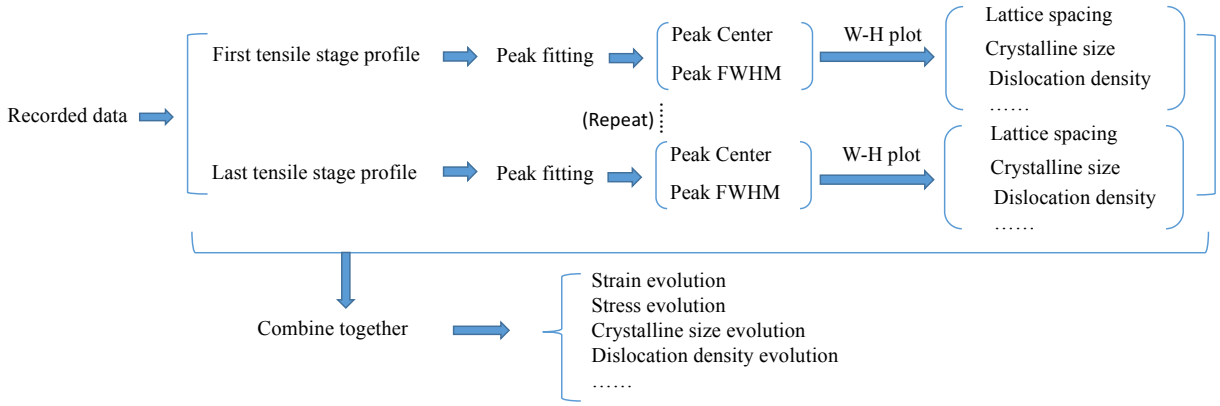

Figure 3.9: Flow chart showing how the recorded data were processed to extract the material related information.

Chapter 4

RESULTS FROM XRD

In this chapter, results derived out of XRD data using methods introduced in Chapter 3 will be discussed in detail. To begin with, macroscopic stress-strain curve will be plotted to calculate mechanical properties such as Young's Modulus. Next, lattice strain evolution and load partitioning phenomenon along with lattice anisotropy effect will be studied. At the end, dislocation density and coherent scattering length evolution trends will also be covered and discussed.

4.1 Macroscopic Stress-Strain Curve

In tensile tests, stress-strain cuve is probably the most used graph to display the responses of materials to outside applied load. In this thesis, in-situ XRD tensile test is no exception. Since there were 3 different temperatures, RT, 450°C, and 550°C, it is a good idea to put them together in one graph for comparison. Due to the limited space around the mini dog-bone shape tensile samples, the actual elongation of the gauge area was hard to measure during on-site synchrotron XRD experiment. We knew the sample gripper movement was the whole sample elongation, which could be transformed to gauge area elongation suppose the gripped area was wide and always within the elastic region. After macro-strain correction, see figure 4.1 for the macroscopic stress-strain curve for T91 steels under 3 temperatures.

From figure 4.1, the UTS and YS of three temperatures can be listed as in table 4.1. It is reasonable to see that both UTS and YS were decreasing with the elevation of experiment temperature. One surprising finding was that instead of being monotonic, the 450°C test had the lowest failure strain compared with the other two, which has also been reported in Ref. [28]. Later in dislocation and coherent scattering length evolution section, it was found that engineering strains at UTS and YS were important turning points. For the convenience of later use, all stress and strain information at UTS and YS are listed in table 4.1 for all three temperatures.

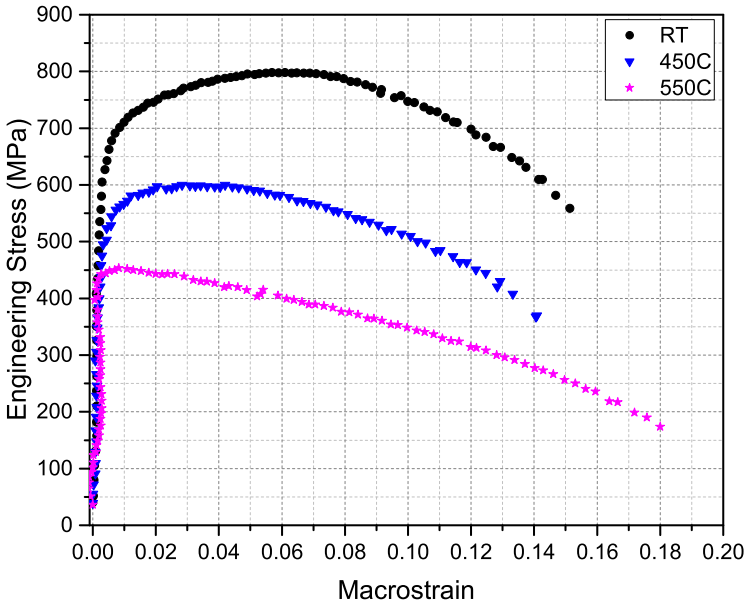

Figure 4.1: Macroscopic stress strain curve for T91 under RT, 450°C, and 550°C.

Table 4.1: Yield strength (YS) and ultimate tensile strength (UTS) (in MPa); macro ultimate tensile strain (ϵ_{UTS}) and macro fracture strain (ϵ_F) for RT, 450°C and 550°C.

Tem.	RT	450°C	550°C
YS	605	497	435
UTS	798	600	453
ϵ_{UTS}	6.1%	3.5%	0.8%
ϵ_F	15.1%	14.1%	18.0%

4.2 Lattice Strain Evolution

As shown in figure 3.2, due to detectors area and experiment setup limitation, only a small number of allowed diffracted rings can be fully recorded. The lattice spacings of these fully recorded diffracted rings are all derived from Bragg's Law. After obtanining all these lattice spacings, paired linear fitting for certain (hkl) plane by d spacing versus macrostress in tensile and transverse directions within elastic regime were made as shown by figure 4.2. The two fitting lines intersections were treated as theoretical zero-stress-state lattice spacings for corresponding (hkl) planes, also used as $d^i_{hkl}(0)^{'}s$ in equation 3.2. The stress of intersection point was not zero due to residual stress left behind by steels cast and sample preparation. For each sample at 0 strain, two planes, Fe(110) and $M_{23}C_6$(422) were selected to use equation 3.1 to calculate lattice parameters of Fe phase and $M_{23}C_6$ phase in T91 as listed in table 4.2.

Applying equation 3.2 on all lattice spacings to form lattice strain variation profile, one can know the response difference of lattice and precipitates to applied load. The selected diffraction planes of Fe matrix

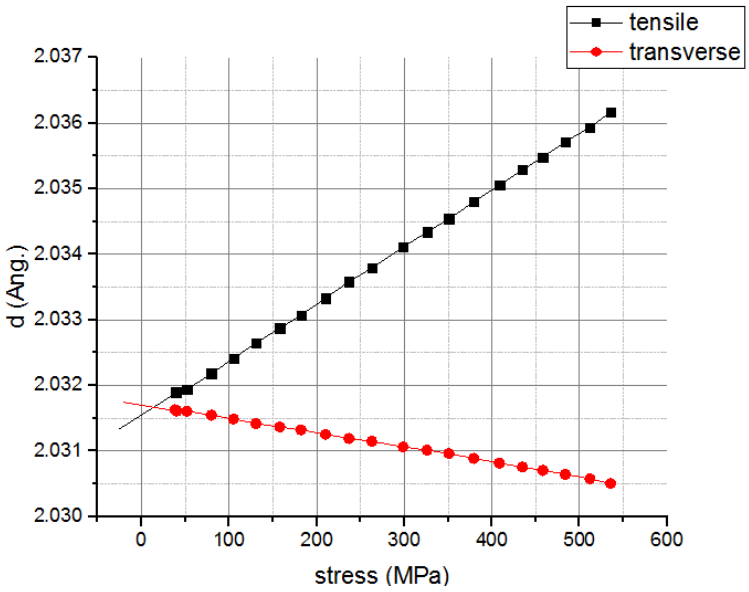

Figure 4.2: Explanation of using linear fitting intersection to find $d^i_{hkl}(0)$.

Table 4.2: Lattice parameters a (in Å) of α-Fe matrix and $M_{23}C_6$ precipitates under RT, $450°C$ and $550°C$.

Tem.	RT	$450°C$	$550°C$
α-Fe	2.873	2.889	2.893
$M_{23}C_6$	10.640	10.690	10.703

were (200), (211), (220), (310), (222), (321), (400) and (330). Besides, two diffraction planes of $M_{23}C_6$ precipitates studied were (422) and (531). As for Nb(C,N) precipitates, their peaks were just too weak to give reliable results, but its behavior was found to be similar to that of $M_{23}C_6$ [19]. Figure 4.3 shows the lattice strain behavior difference choosing 3 Fe matrix planes and 2 $M_{23}C_6$ planes as representatives.

Judging from figure 4.3, before YS strain, the lattice strains of all three Fe matrix lattice planes were increasing linearly, after which they either plateaued for RT or dropped slowly for $450°C$ and $550°C$. As for $M_{23}C_6$ planes (422) and (531), however, their trends were different. After Fe lattice had yielded after YS strain, the lattice strain of $M_{23}C_6$ still went up, ending up with higher lattice strain till sample fracture, especially for lower temperature. This precipitates taking higher strain phenomenon will be revisited again later along with load partitioning (or transfer effect), in which precipitates are taking higher load than the matrix. As temperature increased, it can be seen that this load transfer effect became less obvious noticed that the two curves of $M_{23}C_6$ approached that of three Fe matrix curves at higher temperature. This could be used to explain one of the lower engineering stress reasons at higher temperatures like $450°C$ and $550°C$, precipitates hardening effect generally being weakened by higher temperature.

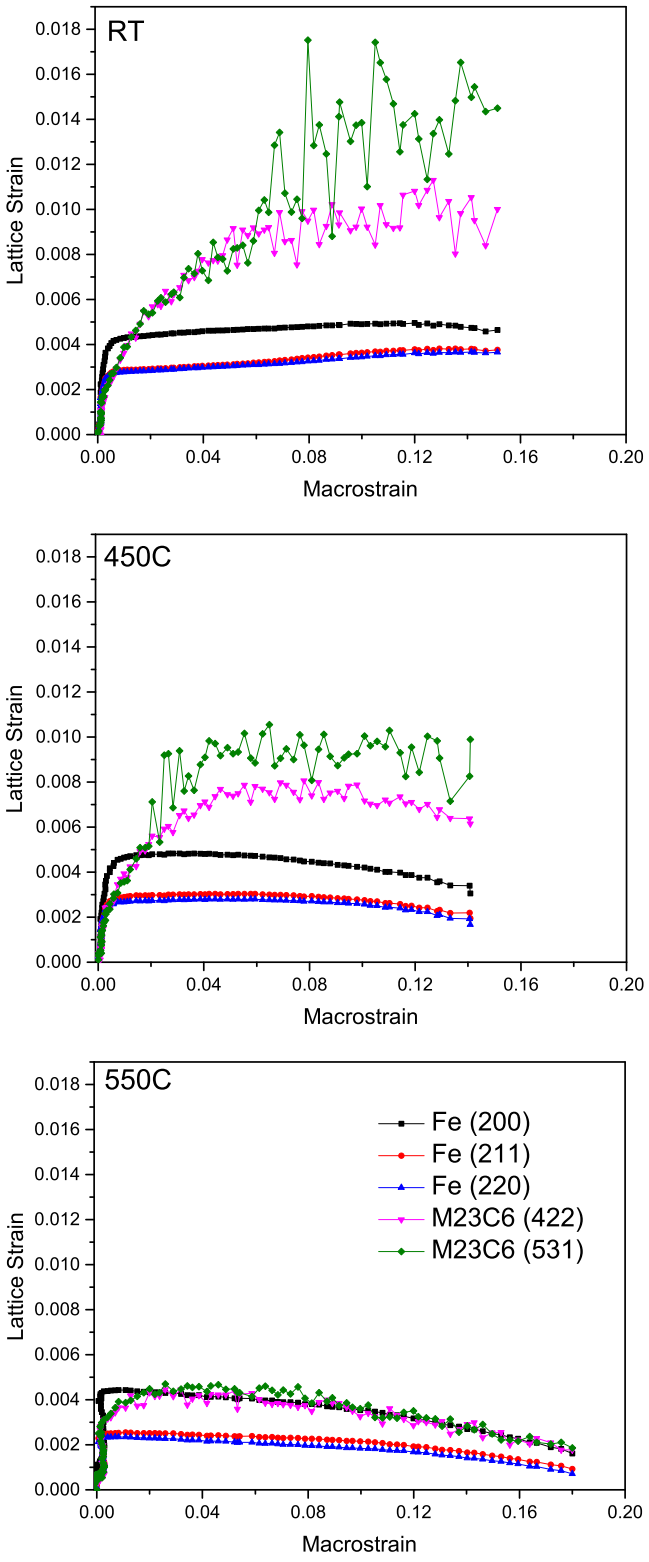

Figure 4.3: Comparison of lattice strain vs macrostrain for Fe-matrix (200), (211), (220) and $M_{23}C_6$ (422), (531) under RT, 450°C and 550°C. With temperature elevation, the lattice strain gap between precipitates and Fe matrix narrowed down obviously.

Another observation is that there were strong fluctuations for $M_{23}C_6$ especially for lower temperture within plastic deformation regime. In addition to tolerable data processing errors, other sources may include lattice fracture or movement and necking center void generation as has been reported in G91 and G92 steels using SAXS technique [18, 19].

4.3 Anisotropy Effect

Young's modulus E and Poisson ratio ν are crucial to reflect bulk material mechanical properties. These values can also be obtained for lattice planes by tensile test using linear fitting of data points before yielding, if assuming that internal stress were isotropic and equaled to engineering macrostress. Table 4.3 lists these values for both tensile and transverse directions for Fe matrix and $M_{23}C_6$. Further stress vs. lattice strain plots can better illustrate this lattice anisotropic properties. From figure 4.4 and table 4.3, easily it can be seen that with the elevation of temperature, Young's moduli for all Fe planes were decreasing. In Ref. [29, 30], T91's temperature dependent Young's modulus can be expressed as equation 4.1.

$$\begin{aligned} E[MPa] &= 207300 - 64.58T[^\circ C], \quad 20^\circ C \leq T \leq 500^\circ C \\ E[MPa] &= 295000 - 240T[^\circ C], \quad 500^\circ C \leq T \leq 600^\circ C \end{aligned} \tag{4.1}$$

Among fitted Fe lattice planes, E of Fe(330) was found to be 204 MPa at RT (about $25^\circ C$), very close to 206 MPa given by the equation above. Also, Fe(330) plane was found to show a good linearity at the start of plastic regime, thus could serve as a good representative for Fe macroscopic stress strain properties. Similarly, (311) plane has been found qualitative to represent engineering properties for FCC materials [31]. Moreover, Fe(200) plane had higher lattice strain but lower Young's modulus than Fe(211) and Fe(220), indicating it was softer than the other two directions. In addition, with the increase of temperature, anisotropy effect was much more obvious evidenced by that profiles split more away from each other for tensile and transverse directions. The T91 Fe(211) properties(E=240, ν=0.27) were nearly identical to that of G92 Fe(211) (E=245, ν=0.27) in Ref. [18] while for Fe(200) and Fe(220) values of T91 were somehow much lower than that of G92 under RT. The latter phenomenon may be explained by composition and lattice preferred orientation differences. Nearly all calculated Poisson ratio ν of Fe diffraction planes were smaller than 0.3, similar to the typical range of 0.25-0.3 for alloy steels.

Similarly, $M_{23}C_6$ was also found to display anisotropic phenomenon by (422) and (531) planes shown in

Table 4.3: Young's moduli E (in GPa) and Poisson ratio ν for Fe and $M_{23}C_6$ planes in tensile (Ten.) and transverse (Tra.) directions assuming isotropic stress inside samples under RT, $450°C$ and $550°C$.

	(RT)		$450°C$		$550°C$	
	E	ν	E	ν	E	ν
Fe(200)Ten.	159	0.25	134	0.31	110	0.27
Fe(200)Tra.	-632		-432		-414	
Fe(211)Ten.	240	0.27	193	0.26	177	0.24
Fe(211)Tra.	-896		-740		-735	
Fe(220)Ten.	230	0.22	195	0.26	181	0.30
Fe(220)Tra.	-1067		-749		-609	
$M_{23}C_6$(422)Ten.	264	0.27	193	0.30	167	0.35
$M_{23}C_6$(422)Tra.	-982		-645		-476	
$M_{23}C_6$(531)Ten.	281	0.30	214	0.36	162	0.33
$M_{23}C_6$(531)Tra.	-936		-599		-492	

figure 4.5. First of all, anisotropy effect for $M_{23}C_6$ was also more obvious for higher temperature like Fe matrix. $M_{23}C_6$ (422) and $M_{23}C_6$ (531) nearly had identical Young's modulus judging from table 4.3 and figure 4.5. However, $M_{23}C_6$(531) was found to have higher lattice strain than $M_{23}C_6$(422) during plastic deformation under RT and $450°C$. Comparing RT, $450°C$ and $550°C$, it is clear that this post-yielding strain anisotropy became smaller with temperature elevation. Nb(C,N) in Ref.[18] and Fe_3C in Ref.[32, 33] were also found to have this post yielding strain anisotropy effect, which was related to dislocation interaction with precipitates surface under different temperatures.

4.4 Load Partitioning Effect

Load partitioning effect refers to the phenomenon that precipitates are taking more load than matrix and von Mises stress (σ_{VM}) is typically used to quantify and compare [18, 19, 33, 34]:

$$\sigma_{VM} = \sqrt{\frac{(\sigma_{11}-\sigma_{22})^2 + (\sigma_{22}-\sigma_{33})^2 + (\sigma_{33}-\sigma_{11})^2}{2}} \tag{4.2}$$

$$\sigma_{11} = \frac{E}{1+\nu}\epsilon_{11} + \frac{\nu E}{(1+\nu)(1-2\nu)}(\epsilon_{11}+\epsilon_{22}+\epsilon_{33}) \tag{4.3}$$

$$\sigma_{22} = \sigma_{33} = \frac{E}{1+\nu}\epsilon_{22} + \frac{\nu E}{(1+\nu)(1-2\nu)}(\epsilon_{11}+\epsilon_{22}+\epsilon_{33}) \tag{4.4}$$

Where $\epsilon_{11,22=33}$ were calculated with equation 3.2, σ_{11} was the principle stress in axial direction while $\sigma_{22=33}$ in transverse direction. These stress values can be obtained by equation 4.3, 4.4 and the schematic

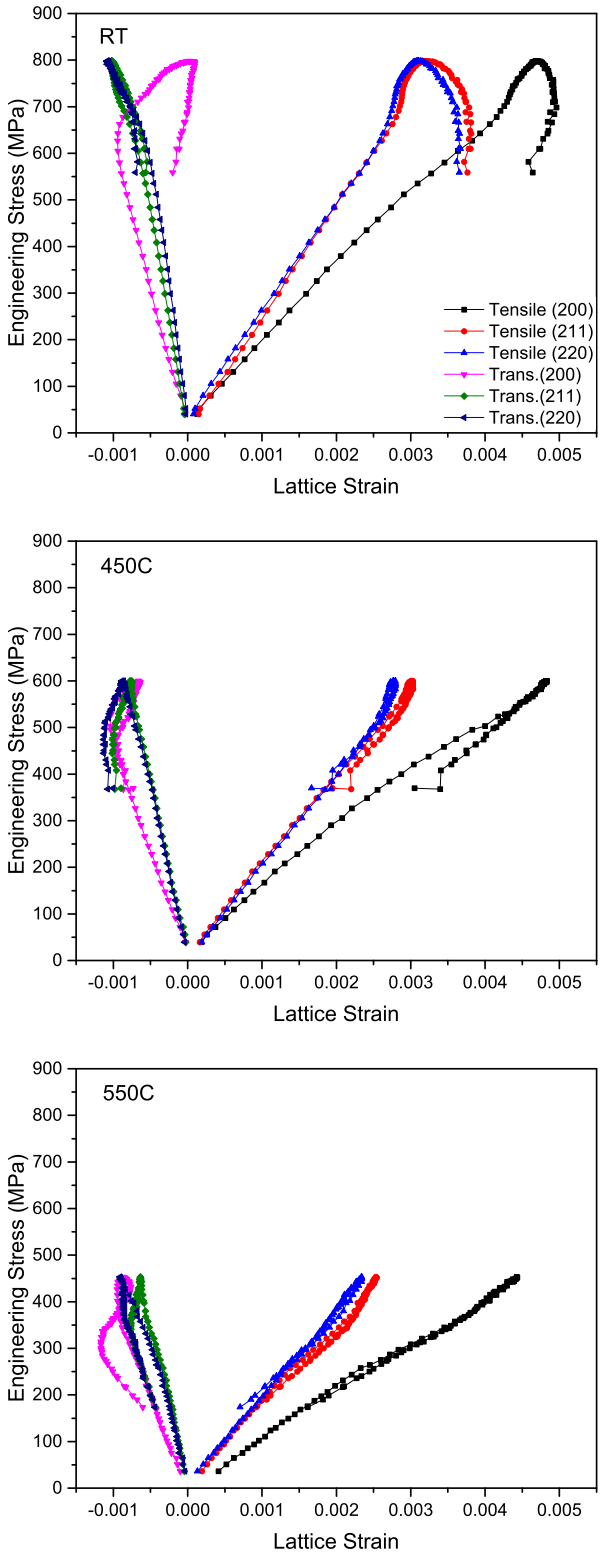

Figure 4.4: Comparison of engineering stress vs lattice strain for Fe-matrix (200), (211), (220) under RT, 450°C and 550°C.

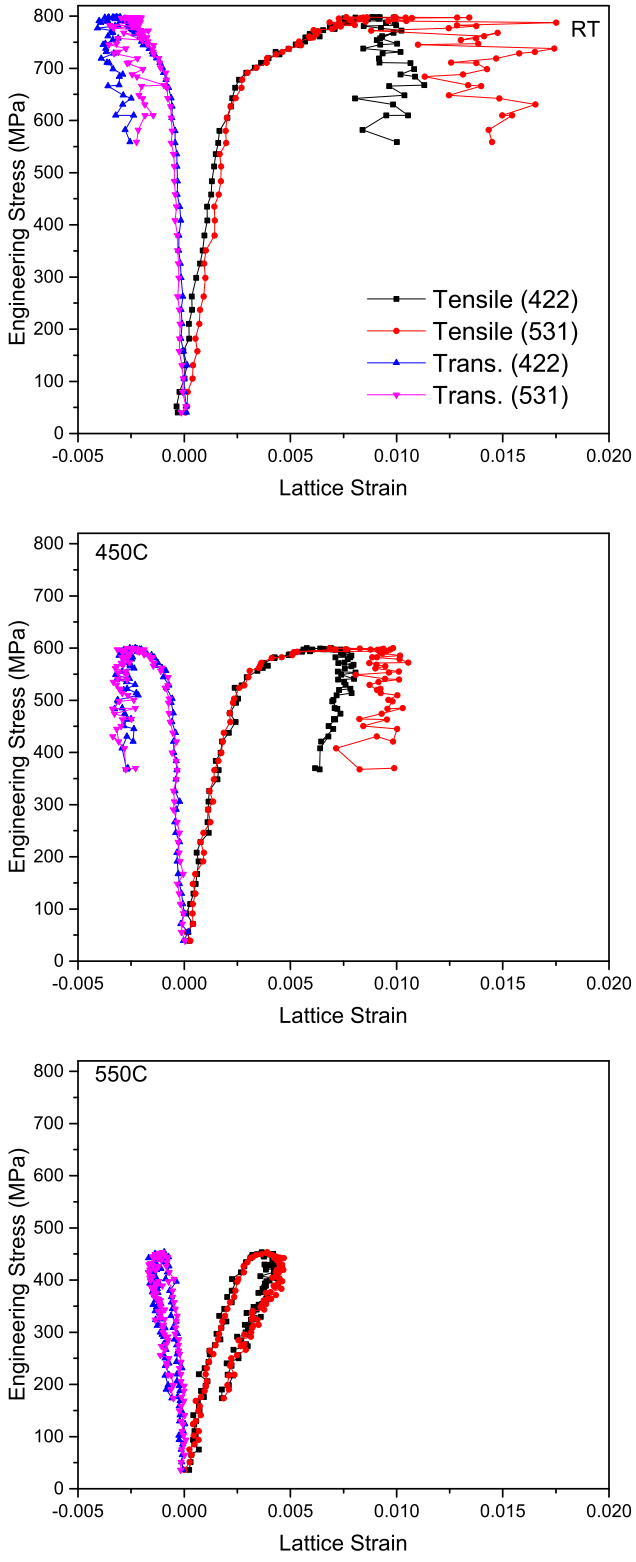

Figure 4.5: Comparison of engineering stress vs lattice strain for $M_{23}C_6$ (422), (531) under RT, 450°C and 550°C.

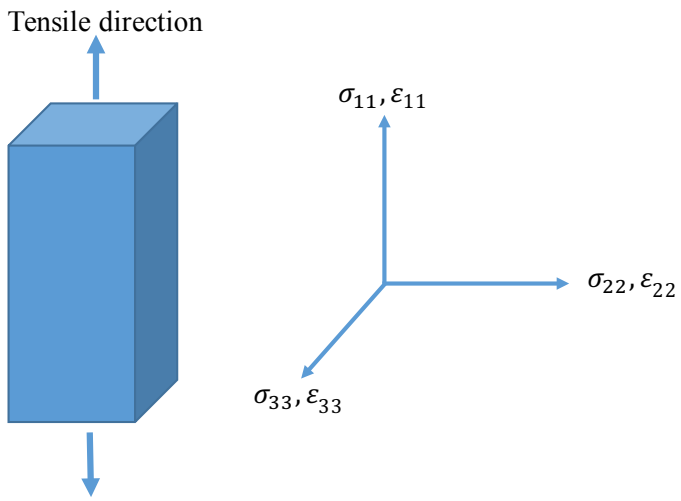

Figure 4.6: Schematic diagram of stress and strain in both tensile and transverse directions.

diagram of these parameters are shown in figure 4.6.

In metals R&D activities, strengthening mechanism is one of the most important factors that help to cast better alloys. Von Mises stress is widely used to evaluate phase stress when study precipitates strengthening mechanism [18, 22]. In this study, Fe(211), (220) and $M_{23}C_6$ (422), (531) were selected for analysis using equations 4.2-4.4 with data from peaks fitting. In figure 4.7, from top to bottom, von Mises stress of Fe(211) basically overlapped with Fe(220) and decreased very little across different temperatures while $M_{23}C_6$(422), (531) decreased intensively with temperature elevation. At RT, the value of $M_{23}C_6$ (422) was several times that of Fe(211) or Fe(220), which indicated that as precipitates, $M_{23}C_6$ was taking more load than the Fe matrix. When temperature went up, the gap between the two phases was narrowing down obviously. At $550°C$, the 4 curves nearly overlapped each other only with a little gap in plastic regime, indicating load partitioning effect was removed away by high temperature. Similar temperature dependent load partitioning effects have been reported in other metals [18, 21, 22]. In terms of T91, this temperature dependent load transfer phenomenon will be discussed along with the variation trends of dislocation density and coherent scattering length in the coming sections.

4.5 Dislocation Density Evolution

Strain broadening and size broadening are two major sources of peak broadening, which can be separated using modified W-H plot as explained in Chapter 3 with equation 3.6. Generally, strain broadening is related

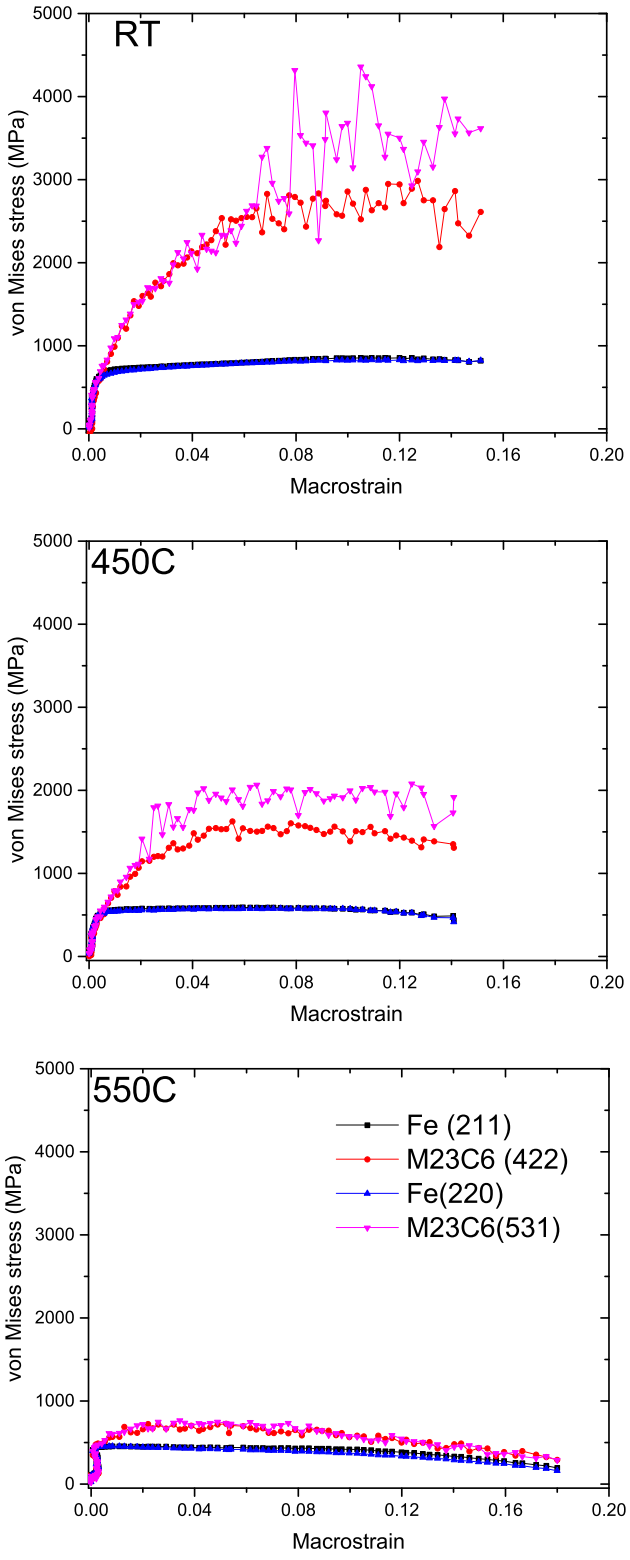

Figure 4.7: Comparison of von Mises stress vs. macrostrain for Fe(211), Fe(220) and $M_{23}C_6$(422), $M_{23}C_6$(531) under RT, 450°C and 550°C.

to dislocation density while size broadening can exploit crystalline size information. Traditional W-H plot uses FWHM (usually in radian) vs. diffraction vector length g_{hkl} (usually in nm^{-1}) from different (hkl) planes of selected phase [19, 24]. The linear regression fitting y-intercept equals to inverse of weight averaged crystalline size while the slope is proportional to the square root of average dislocation density. However, calculation showed that FWHM is not monolithic with diffraction vector length g_{hkl}, resulting in low R^2 for linear regression fitting. Other research [35, 36] have found that if introducing dislocation contrast factor (C) decided by microscopic particle geometric properties, modified W-H plot using equation 3.6 can give out better fitting then. In this study, contrast factor C used 50% edge dislocations $\{110\} < 111 >$ and 50% screw dislocations $< 111 >$ data from Ref. [19] as in table 4.4.

Table 4.4: Dislocation contrast factor C for diffraction *(hkl)* planes in Fe-matrix assuming (a) all dislocations are edge type 110<111> as C_E; (b) all dislocations are screw type $< 111 >$ as C_S; (c) all dislocations are half edge type 110$< 111 >$ and half screw type $< 111 >$ as C_{ES}. Table taken from table 3 in Ref. [19].

	(200)	(211)	(220)	(310)	(222)	(321)	(400)	(330)
C_E	0.262	0.178	0.178	0.232	0.150	0.178	0.262	0.178
C_S	0.304	0.104	0.104	0.232	0.037	0.104	0.304	0.104
C_{ES}	0.283	0.141	0.141	0.232	0.094	0.141	0.283	0.141

Figure 4.8 showed the dislocation density ρ evolution profile in Fe-matrix at different tensile strain under three different temperatures. The magnitude of dislocation densities were initially in 3 - 4 $\times$ 10^{14} m^{-2}, a little bit higher than normal range of other F/M steels in Ref. [19, 37, 38]. This results can arise from several sources. On one hand, the sample preparation processe may differ from others, which matters a lot. On the other hand, the error bars are relative huge to true values on this figure, suggesting the noise added in during data aquisition, processing and fitting steps. In this situation, we should pay more attention to dislocation density variation trend versus strain. Before UTS (ϵ=6.1% for RT, ϵ=3.5% for 450°C and ϵ=0.8% for 550°C), ρ increased for all three temperatures. After UTS, ρ stabled then climbed again at about ϵ=12% for RT; plateaued continuously until fracture for 450°C; decreased all the way to fracture for 550°C. Generally, temperature and tensile tension are two competing factors affecting the internal dislocation density of Fe-matrix. High temperatures tend to enhance dynamic dislocations migration and annihilation [19] while tensile induced flow stress will support its generation predicted by Taylor equation 4.5.

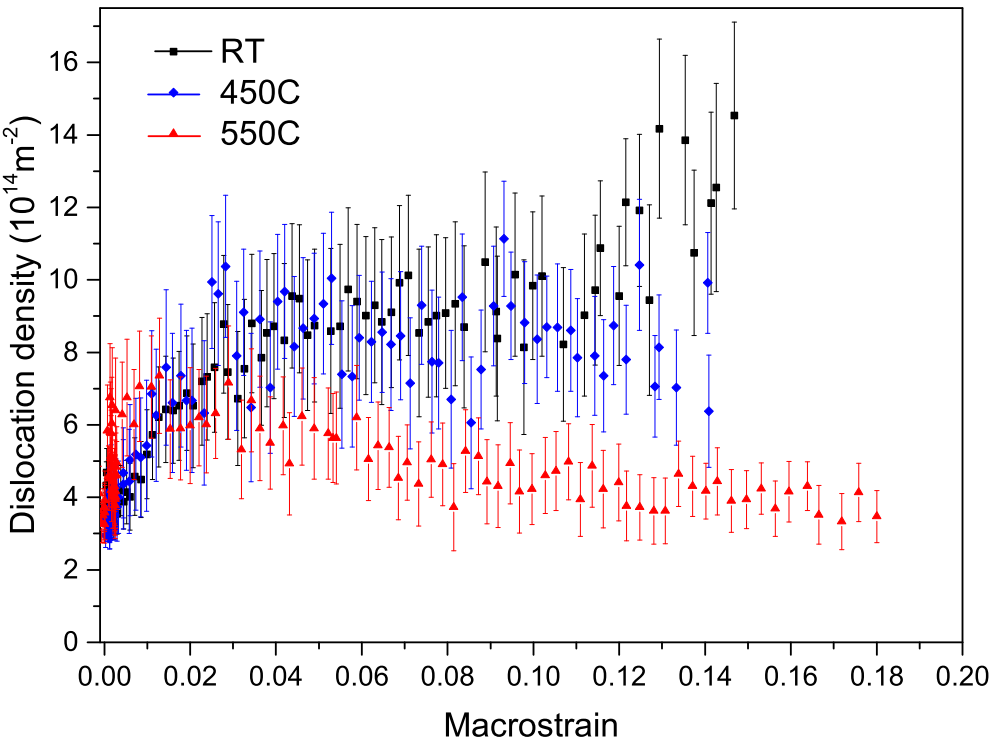

Figure 4.8: Dislocation density evolution profiles calculated from modified W-H plots under (RT), 450°C and 550°C. Nearly all the R^2 for least square fitting were higher than 0.90 to ensure good fitting.

$$\sigma = \sigma_0 + M\alpha G b\sqrt{\rho}. \tag{4.5}$$

Where M is Taylor factor, which could be taken as 3; G is shear modulus; b is Burger's vector and α is a factor about 0.3. In this experiment, the early elastic regime before YS witnessed stable and similar dislocation densities under different temperatures evidenced by densely overlapped data points at the very beginning. In this regime, the flow stress was low and the high temperature effect enabled $450°C$ and $550°C$ with a little bit smaller value at the very beginning than that of RT. Between YS and UTS, flow stress increased linearly with square root of dislocation density predicted by Taylor equation. In this period, ρ increased at different rate for the three curves. The overall trend is that the higher the temperature, the faster the ρ climbed. After UTS, thermal migration and dynamic elimination prevailed, and dislocation density stabled for $450°C$ but dropped for higher $550°C$. The abnormal increase of ρ under RT near failure point may be explained by dislocation multiplication activities induced by inner cracks and sudden fracture, which can be seen by SEM fracture surface observation, or just becasue of calculation errors.

4.6 Coherent Scattering Length Evolution

Generally, crystalline size is different from particle size due to polycrystalline aggregates formation [39]. XRD based W-H plots or size-strain method can obtain the weight averaged values for crystalline size [24]. Due to the fact that standard sample Ceria (CeO2) used as standard sample to account for instrumental broadening may still have some self broadening, resulting in instrument broadening overcorrection, modified W-H plots gave out some negative, not physically reasonable y-intercepts as in figure 3.8. Since precise averaged crystalline size could not be obtained by modified W-H plots if there exists broadening overcorrection, Scherrer equation 3.7 can be a compromise or substitution if only some length scale variation trend related to particle or grain size is needed. This equation was discussed and corrected in Ref [40], and can be used to calculate the structural coherent scattering length along the $< hkl >$ direction for given (hkl) diffraction plane. For this thesis, Fe(310) plane was chosen as a representative to plot and discuss.

Scherrer equation calculation used single profile assumption, attributing Gaussian component solely to strain broadening and Lorentzian component solely to size broadening [27]. The results of coherent scattering length L_{310} are shown in figure 4.9.

The initial magnitude of L_{310} was of a few hundred nanometers, smaller than the size of grain, which was found to be around 20 μm by metallographic observation later. By definition above, coherent scattering length L_{hkl} should be smaller than grain size given the existence of subgrains. As explained before in dislocation evolution section, due to systematic errors and calculation errors, attention should be paid more to variation trend of L_{310}. For RT, 450°C and 550°C, profiles had a plateau until their own YS featured by those densely overlapping dots at beginning, after which L_{310} shrank at different rate between YS and UTS. After UTS, L_{310} continued to shrink at lower rate for RT, came to a platform for 450°C and increased steadily for 550°C. Even though higher temperature generally would facilitate grain growth, early L_{310} stage of 450°C and 550°C were a little bit lower than that of RT. It could be due to sample preparation process or be explained as higher temperature would make grains softer, easier submitted to induced fracture by internal stress. Also, grain orientation and configuration within different samples could be different. As temperature went higher, the subsequent work softening regime saw increasing tendency for coherent scattering length. For 550°C sample, final L_{310} was even higher than that of pre-test status. During work hardening and softening process, higher temperature test (450°C and 550°C) could only bear lower stress than lower temperature test (RT) as in figure 4.1, thus internal flow stress effect was in inferior and subgrain boundaries thermal disappearance to create larger grain dominated L_{310} variation trend.

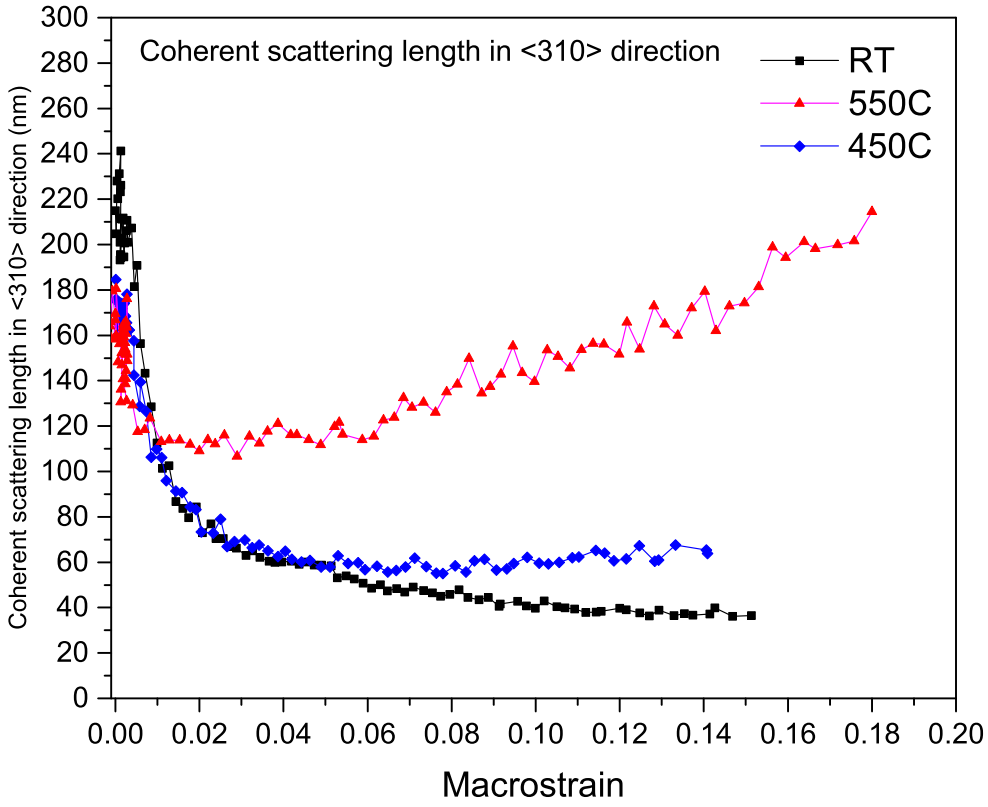

Figure 4.9: Coherent scattering length L_{310} calculated using Fe(310) diffraction plane and Scherrer equation under RT, 450°C and 550°C. L_{310} is different from weight averaged crystalline size D_v, but it can still be used to capture some overall trends of crystalline-related size variation.

Another finding is that different (hkl) planes such as Fe(200), Fe(321) gave out different L_{hkl}. The equation 3.7 in fact returned the structural coherent scattering length along the $< hkl >$ direction. It suggested that T91's coherent scattering volumes (or grain) were far from spherical shape and grains have preferred growth orientation, asking for further experiment verification using techniques such as EBSD. L_{hkl} is different from D_v, but it still represented a type of length scale variation trend, which could be comparable to that of crystalline size evolution process. Lastly, it would be a good idea to plot the normalized dislocation density evolution profiles and normalized coherent scattering length evolution profiles. Even though came from a same batch and went through same processings, the three temperature samples for tensile test still had differences to each other. Normalized profiles help us to concentrate on the variation trends better.

Chapter 5

MICROSCOPY STUDY

In this chapter, microscopy observations of post tensile samples were conducted to study the effect of tensile tension on microstructure evolution. In the first section, Scanning Electron Microscopy (SEM) was used to study the fracture surface morphology, followed by SEM/Energy Dispersive Spectroscopy (EDS) to see chemical element distribution. Next, chemical etching and Optical Microscopy (OM) was performed to reveal the grains and boundaries in section two. At the end, this thesis included Transmission Electron Microscopy (TEM) work to study dislocation density, grain morphology and precipitates.

5.1 SEM Study of Fracture Surface

Tensile test under different temperatures, namely, RT, 450°C, and 550°C in this study, behaved differently juding from the stress-strain curves and other diverse results shown in Chapter 4. Lower temperature test was found to show lower strain but more obvious load partitioning effect while higher temperature test generally was just the opposite. In order to fully understand the difference there, it is necessary to study the characteristics of those post-tensile samples from several perspectives. First of all, before adding any post-processing to damage these samples, the pure observation of fracture surface was easy and ready to go.

SEM is a traditional but state-of-the-art technique which uses scanning electrons to hit the samples surface. The induced secondary electrons emitted by sample atoms will be collected by detectors. The number of collected electrons depends, among other factors, on specimen topography [41]. In this study, two SEM working modes were used, one was Magnetic Sample Mode (T91 is ferromagnetic) to collect the surface morphology image while another one was EDS Mode to obtain the chemical element distribution information. Figure 5.1 shows how SEM was used to observe the fracture surface in the SEM chamber. Electron beam hit the sample in the direction from outside the paper into the paper.

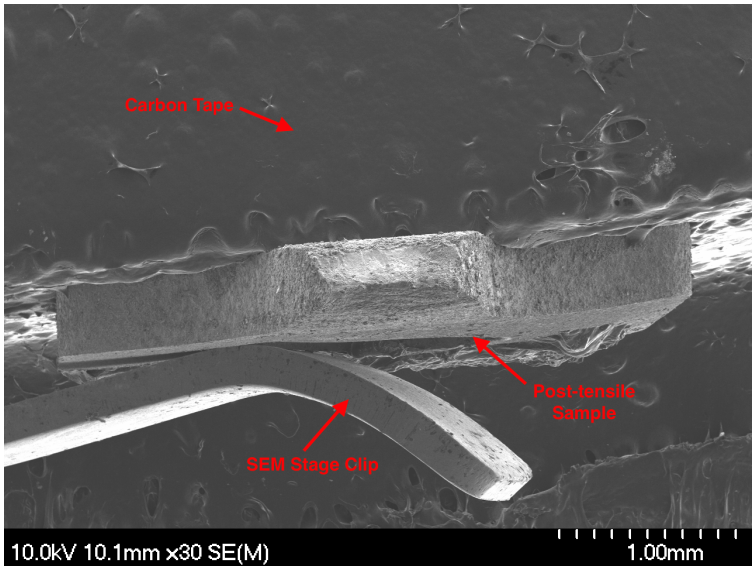

Figure 5.1: SEM experiment overview of the T91 post-tensile sample. Carbon tape and SEM stage clip were used to hold the sample tightly on the stage because T91 is ferromagnetic and will be attracted by the electron beam. This graph was taken with 30 magnification for the 450°C sample just as an example.

SEM is capable of observing tiny features as small as subnanometer these days in material sicence field. In this study, samples were observed under several selected magnification to fully compare their differences. Figure 5.3 enlarged the samples 1000 times while the magnification of figure 5.4 was 5000.

In Figure 5.3, easily it can be seen that the three samples of the same 1000 times magnification displayed distinctive features. For the first lower temperature sample at RT, several huge cracks and cleavages were found in the captured scope as well as for all other areas within the necking center. Second figure for the 450°C had far less cracks but exhibited some shadow dimples and holes. The last 550°C surface was similar to that of 450°C but with deeper holes and small particles. As the magnification went higher to 5000 as in figure 5.4, much more details were disclosed. As shown in figure 5.4, the RT sample fracture surface rise and fall, still with cleavages and nano cracks induced by tensile tension. For 450°C sample, its surface was relatively flat, still with some cracks left and shadow dimples showed up. When the temperatue went up to 550°C, the surface dimples went deeper with holes, also decorated with small particles pointed with red arrows.

In strain-stress curve of figure 4.1, RT sample was subject to higher stress but withstood smaller fracture strain, while 450°C and 550°C beared lower fracture stress, producing longer fracture strain. SEM images also proved that RT sample had larger final fracture cross-section than that of higher temperatues. During

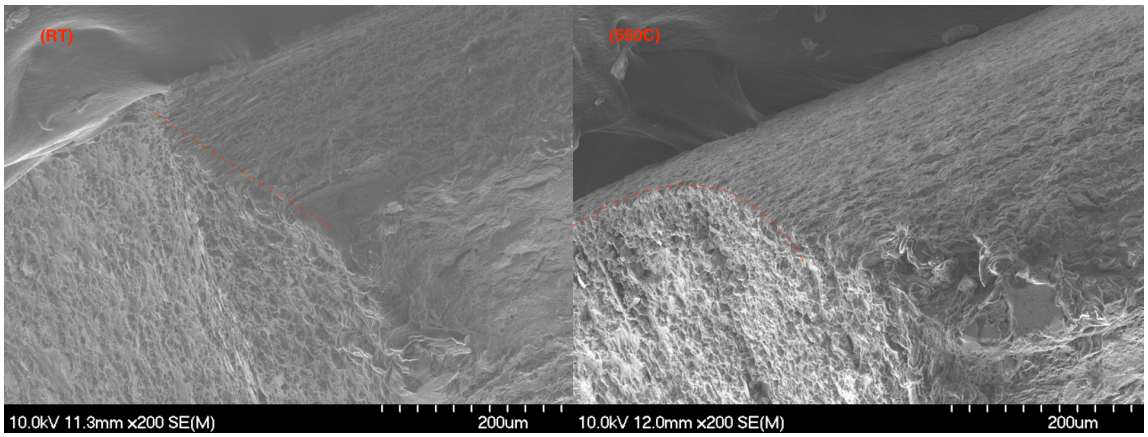

Figure 5.2: SEM fracture corner showing deformation differences for RT and 550°C samples. In the left figure, the short red dashed straight line hinted the violent necking process to fracture while the long red dashed arch shape line depicted the slow necking process under higher temperature in the right figure. The corner of 450°C sample was not listed here becasue it was in between the trend of that of RT and 550°C.

tensilie test, the strain rate was fixed to 2×10^{-4} s^{-1}, thus smaller fracture strain of brittle RT sample corresponded to shorter test time, and more violently fracture. On the contrary, for 450°C and 550°C samples, higher temperature made samples more ductile, enabling longer strain, smaller final cross-section, and gradual fracture. Figure 5.2 included the necking center corner of RT and 550°C, showing their deformation differences. In a word, SEM fracture surface observations agrees with XRD results very well.

In figure 5.4, small particles were found for the 550°C sample. In order to validate whether they are secondary phase precipiates or just tiny Fe matrix particles, SEM/EDS was applied to study the composition or element distribution of the fracture surface. Previous literature have shown that $M_{23}C_6$ (Where M is mostly Cr) and MX (Where M can be Nb or V, X can be C and N) precipitates can be found in G92 steels [18, 42]. Similarly, EDS can see if certain elements formed clusters in the studied areas. Due to time and effort limitation, EDS was performed only on the 450°C sample as results shown in figure 5.5.

5.2 OM Study of Grains

Without introducing any modification to the samples, the fracture suface of post-tensile samples were inspected by SEM in the previous section. The next step is to use metallographic observation to study the physical structure and chemical component of metallic alloys using Optical Microscopy (OM) in this section and Transmission Electron Microscopy (TEM) in next section after certain steps of sample preparation.

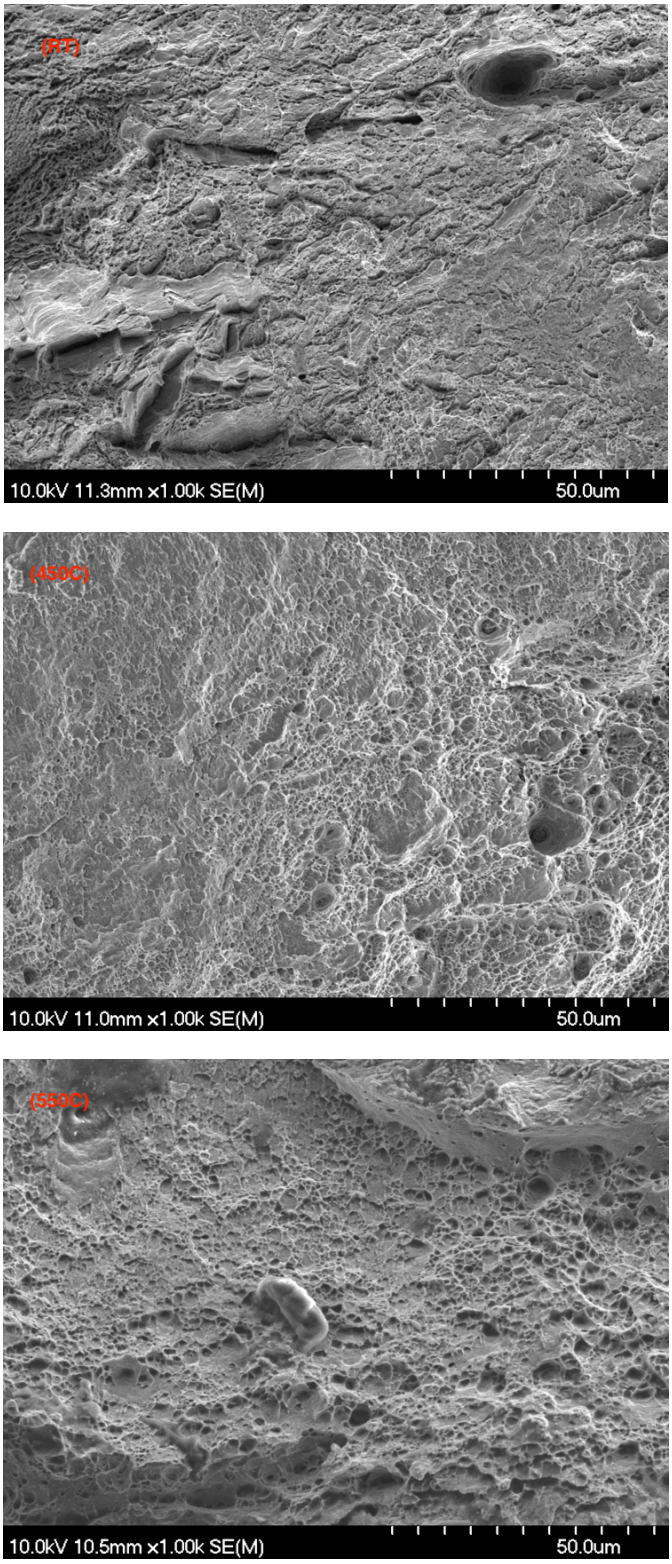

Figure 5.3: SEM 1000 times magnification of post-tensile samples under RT, $450°C$ and $550°C$. RT sample was featured by cracks and cleavages, while $450°C$ and $550°C$ samples displayed more holes, voids and dimples.

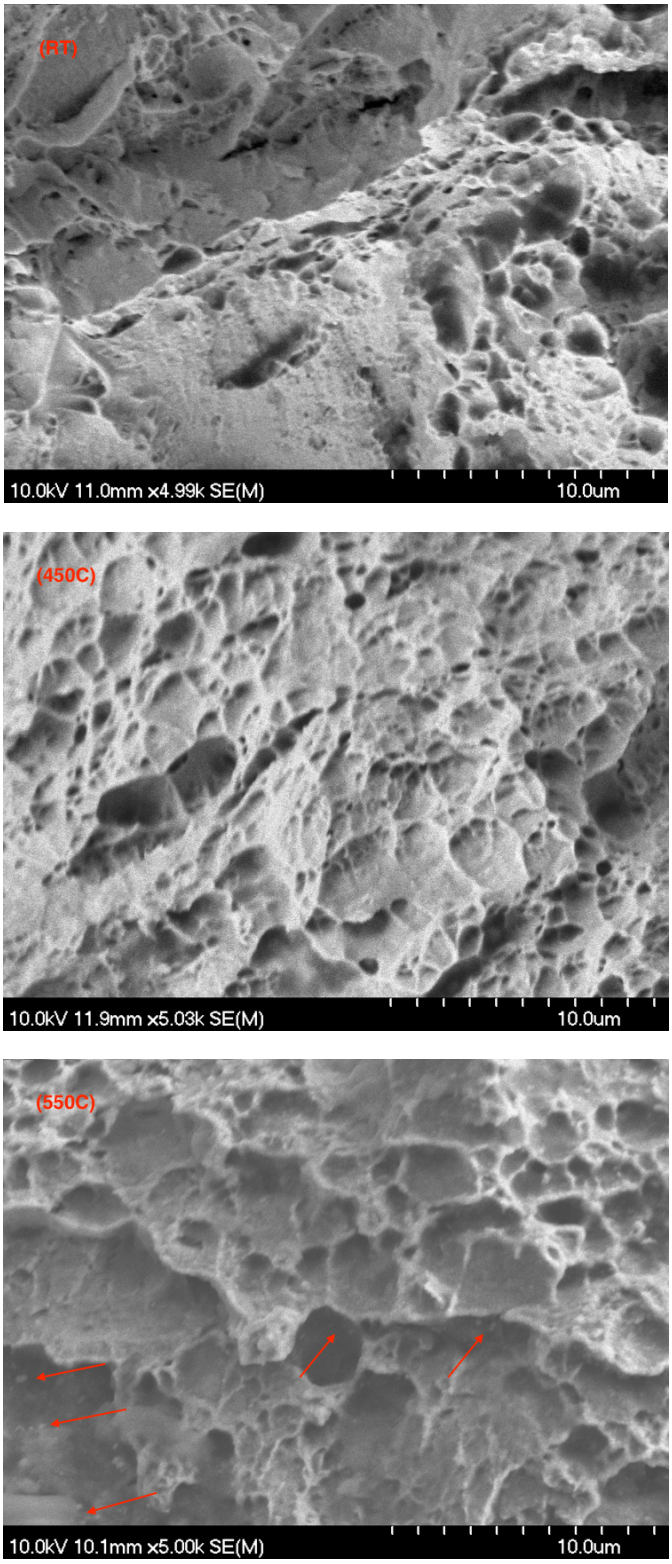

Figure 5.4: SEM 5000 times magnification of post-tensile samples under RT, $450°C$ and $550°C$. RT sample was still featured by small cracks and cleavages, $450°C$ sample showed shadow hole and dimple while $550°C$ samples had deeper holes with the appearance of secondary phase particles pointed by red arrows.

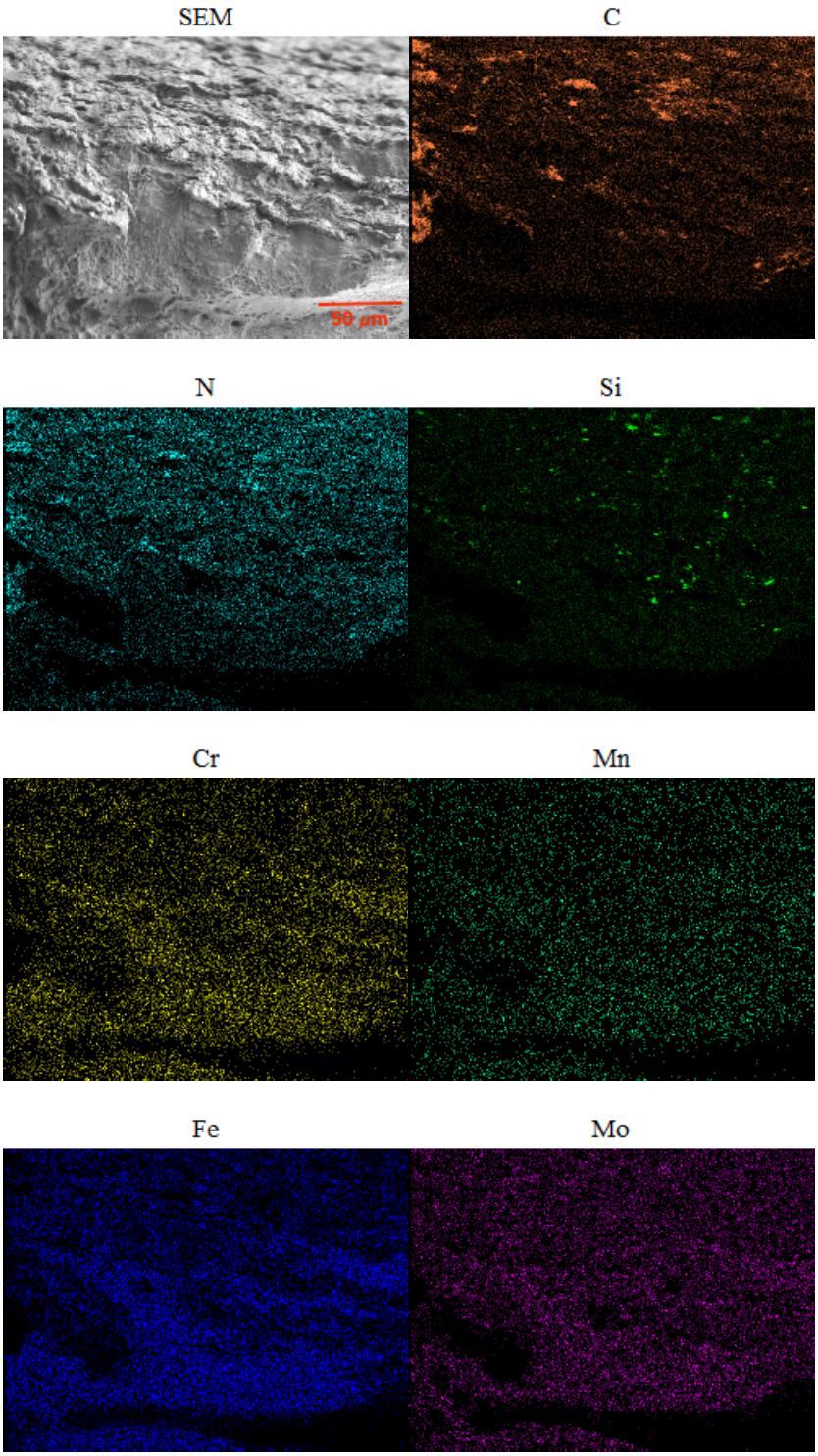

Figure 5.5: SEM EDS composition mapping from one edge area of necking center by $450°C$ sample. Left and upper protrusions from surface cracks are enriched in C and N. Si formed some clusters at the right and top parts where the C and N were less concentrated. Cr, Mn and Mo were nearly uniformly distributed with very small shiny clusters on their maps. Fe is the base element, behaved similarly to that of the other metal elements.

In this study, post-tensile samples were grinded sequentially using BUEHLER 180, 400, 800, 1200 SiC grit paper and polished by 3 μm and 0.05 μm Silica diamond suspension. After grinding and polishing, chemical etching using 7% nital solution [43] or marbles reagent [44] was performed to etch the grain boundaries to reveal the metallic phases as in figure 5.6 taken 550°C sample as an example.

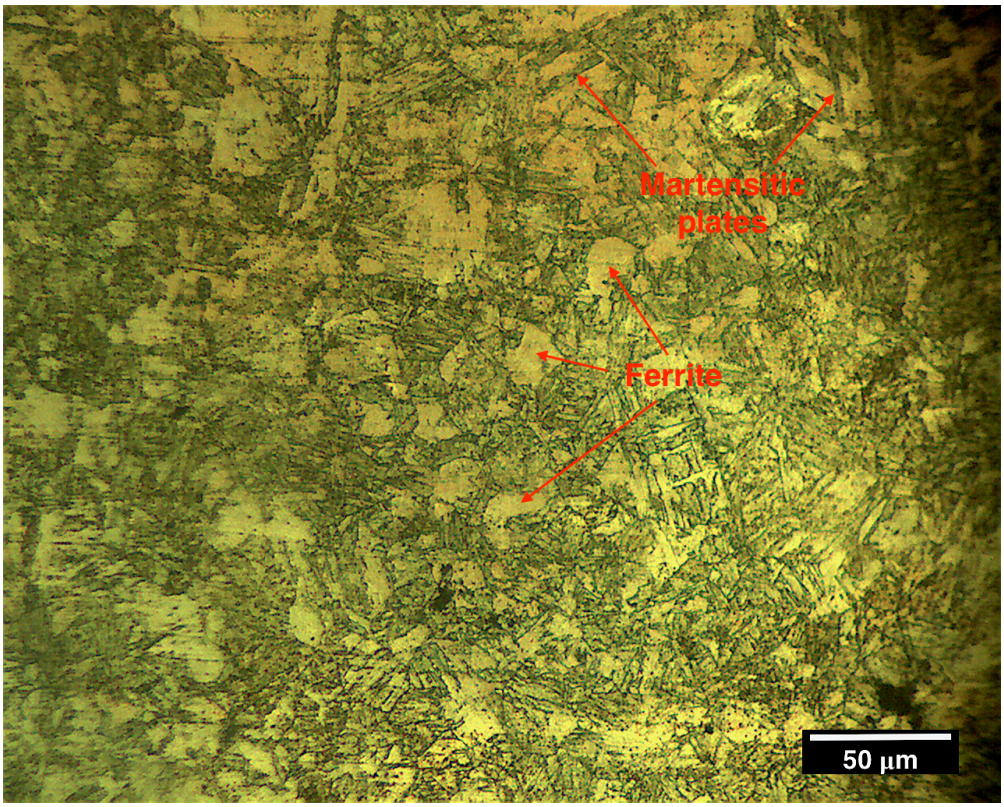

Figure 5.6: Zeiss Optical Microscope 200 magnification observation of 550°C sample after grinding and etching. The sample was a little bit over etched. White areas represent ferrite phase while dark plates belong to martensitic phase [44].

T91 F/M steels in the figure showed typical martensitic plates as well as ferrite phase under the optical microscope. However, XRD calculation results in previous chapters and other literature also showed the existence of precipitates such as $M_{23}C_6$ and MX in T91 variations. These microstructure features are generally beyond the reach of common OMs, thus TEM will be used to handle that.

5.3 TEM Study of Dislocation, Grains and Precipitates

TEM is a modern, powerful tool for investigating the microstructure of materials such as metals, alloys, ceramics, polymers, ceramics, etc [45]. Due to the shorter wavelength of high energy electrons than visible light, TEM has higher resolution and thus can be used to study even finer details, sometimes to the atom level. In principle, transmitted electron beam and diffracted signals can be collected by detectors to analyze and predict the structure of the sample. Weak Beam Dark Field (WBDF) technique is widely used to quantify the dislocation density in materials. In this study, post-tensile samples were used to make TEM specimens. Since T91 post-tensile samples were too small to cut with electric saw, Focus Ion Beam (FIB) technique was used to lift a tiny TEM specimen out of the $450°C$ sample only, due to instrument time limitation.

In addition to martensitic laths and ferrite found in TEM overview, precipitates, seen as dark spots on figure 5.7, also showed up. After enlarged, these precipitates are shown in figure 5.8. Blue circle line enclosed the intragranular precipitates while the red dashed circle encircled the intergranular precipitates.

Moreover, by tilting the specimen into certain zone and direction, TEM can give the information about the dislocation density inside the T91 post-tensile samples as shown in figure 5.9. One disadvantage of preparing TEM specimens using FIB technique is that high energy ions bombardment and too small final thickness may cause the specimens easy to bend. If bending ever happend, diffraction conditions of adjacent areas would be different. This single TEM specimen was prepared by FIB using 4 hours, with 3 mm by 1.5 mm area but only 60-100 nm final thickness, thus subject to bending and deformation between the time interval of FIB and TEM experiment. As shown in figure 5.9, due to possible bending and uneven beam intensity effect, the diffraction conditions of the sides and center were slightly different, causing different contrast of dislocations to the Fe matrix. The dislocation lines in the center were wider and brighter (or darker) than that of the side areas in WBDF image. Those side effects may introduce minor errors to analyze the dislocation density based on TEM WBDF figures, but it is still doable in order to compare with the XRD fitting results in Chapter 4. Future better TEM sample preparation is required to quantify more reliable dislocation density value based on TEM imaging technique.

With the TEM BF and DF dislocation images above, it is feasible to count the dislocation density in the sample. From subfigure (B) in figure 5.9, five different areas with total area about $4.80 \times 10^{-13}\ m^2$ were selected to count the number of dislocation lines. In each area, the upper and lower bound of the number of

dislocation lines were counted, averaged and then divided by the area to calculate the dislocation density of this area. At the end, the results of five selected areas were averaged again and used one standard deviation as the error bar. After all these steps, the calculated dislocation density in this $450°C$ specimen was $6.26 \pm 0.21 \times 10^{14}\ m^{-2}$.

In fact, images in figure 5.9 were taken in the [011] Zone with g = 110. Only Burger's Vectors $\vec{B}$ that satisfied $\vec{g} \cdot \vec{B} \neq 0$ can be seen in figure 5.9. After checking each $\vec{B}$ in $< 111 >$ family one by one, it was found that only 4 out of 8 dislocations types were visible in figure 5.9, which meant that the true value of dislocation density should be double of that value above, $1.25 \pm 0.42 \times 10^{15}\ m^{-2}$ as the corrected value. In figure 4.8, the XRD final calculated dislocation density for $450°C$ at fracture by W-H method was around $1.0 \pm 0.1 \times 10^{15}\ m^{-2}$, very similar to the TEM corrected results above. Again, this proved that the XRD results agreed well with microscopy work.

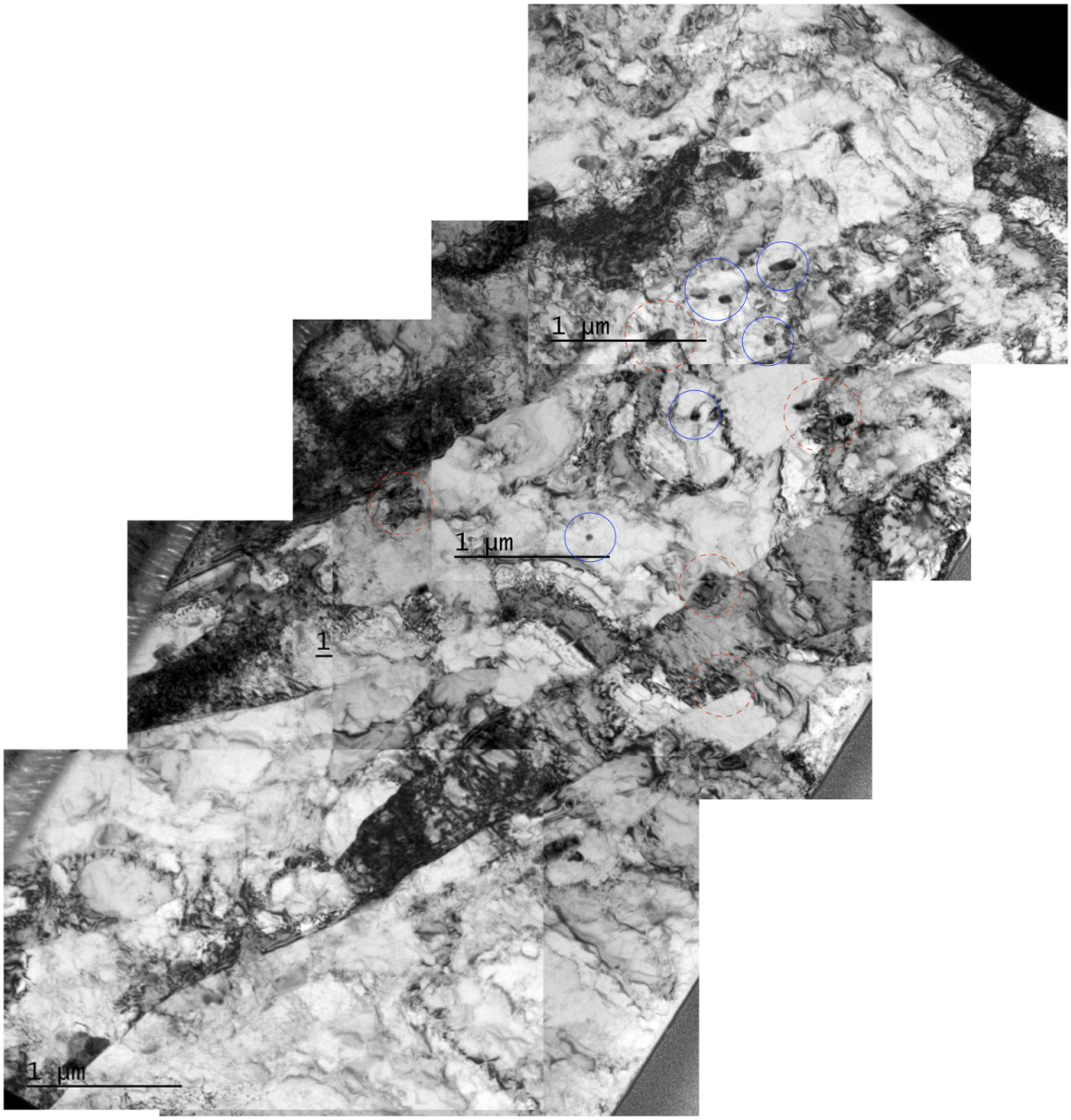

Figure 5.7: TEM overview of the $450°C$ specimen showing martensitic lath, ferrite and precipitates. This whole figure was made up with 7 sub figures, and their magnification was 8000. The martensitic lath size were large than that of G91 steel in figure 1 of Ref. [19], and with subgrains inside them.

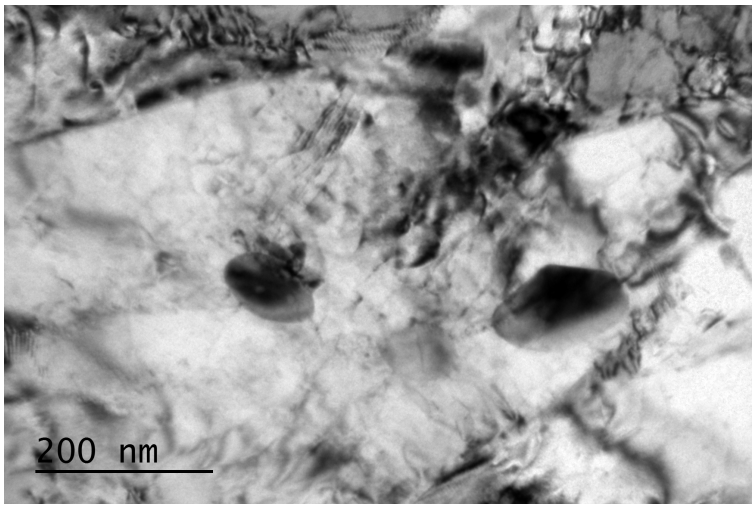

Figure 5.8: TEM capture of two precipitates under 30,000 magnification from figure 5.7. The size of the two precipitates was about 50 to 150 nm from the scale bar.

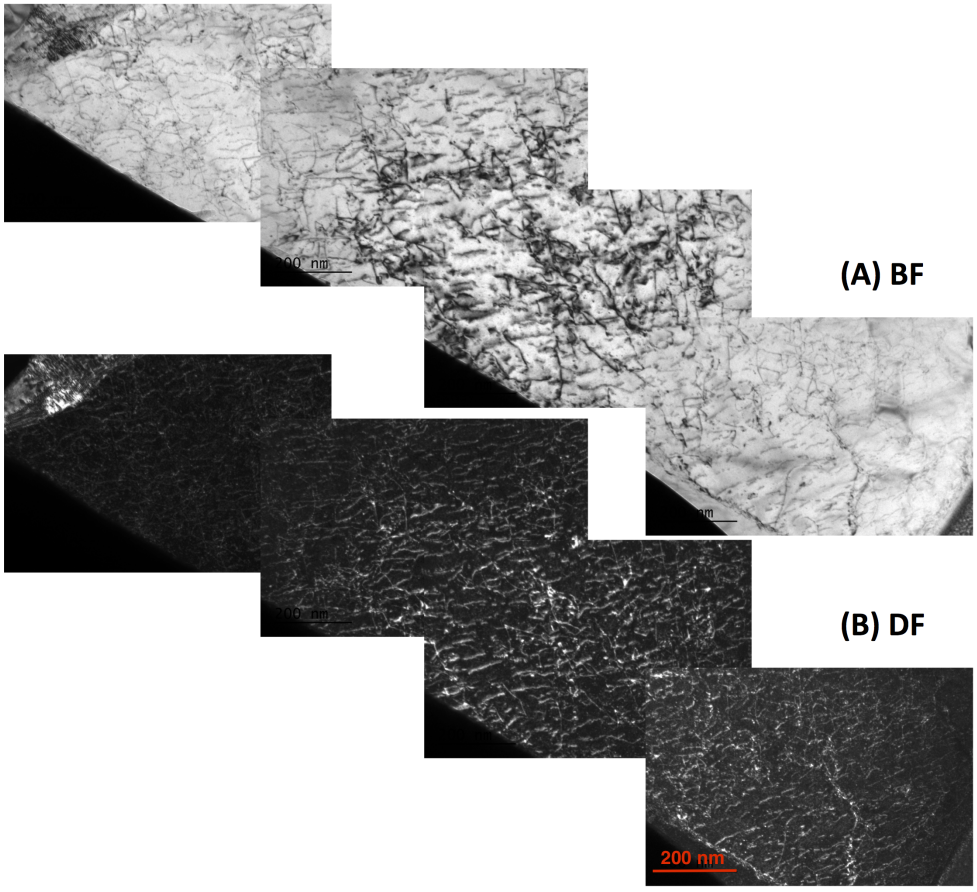

Figure 5.9: (A) TEM Bright Field (BF), and (B) Dark Field (DF) images of dislocations under 30,000 magnification. The images were taken in the [011] ZONE. In the FIB made specimen, the center area diffraction condition was slightly different from the two sides, leaving wider, darker (in A) or brighter (in B) dislocations lines behind.

Chapter 6

DISCUSSION AND COMPARISON

In this study, T91 was studied under in-situ XRD tensile test. Since it's variants G91 and G92 have been investigated by similar techniques in literature already, it is meaningful to compare the results of T91 from this study with that of G91 and G92. This chapter will discuss their similarities and differences due to minimal element concentration change, from several aspects.

6.1 Macroscopic Stress Strain Performance

The elements of T91, G91 and G92 have been listed in table 2.1 previously. Basically, their difference is that only T91 has 0.4 wt.% Si and 0.6 wt.% Mn included, and the concentration of Nb and N varies a little bit. Other major elements' weight percentage like C, Cr Mo are basically the same. G91 XRD tensile test was reported in Ref. [19] under RT and 650°C, while G92 was studied in Ref. [18] under RT, 400°C and 650°C. The Stress-Strain curve of all these three Fe are similar, also like ex-site tensile test results.

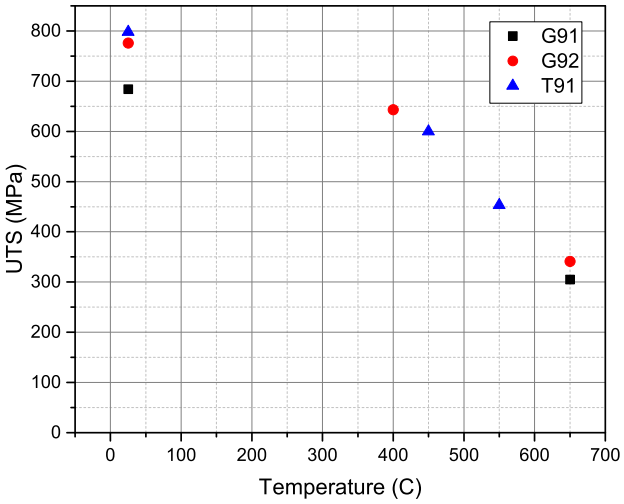

Figure 6.1: UTS of G91, G92 and T91 VS. temperature. G91 and G92 data points were retrieved from Ref. [19, 18].

From figure 6.1 it can be seen that with the elevation of temperature, the overall UTS trend for the 3 Fe

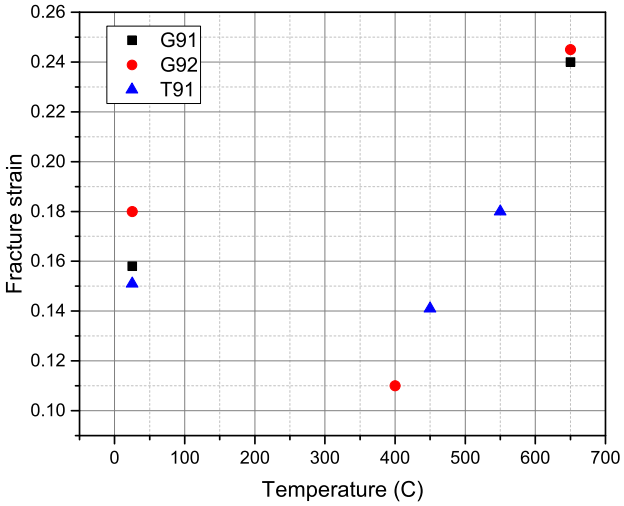

Figure 6.2: Final fracture strain of G91, G92 and T91 VS. temperature. G91 and G92 data points were retrieved from Ref. [19, 18]. G92 at RT and G91 at 650°C data points were extropolated from figures in references cited.

variants are decreasing just as expected. High temperature generally tend to soften materials and limit their applications into environments with high temperture requirement. G91 had the lowest UTS at RT, 100 MPa lower than the other two, which can be attributed to the elemental difference and sample treatment difference.

On the other hand, the overall tendency of fracture strain VS. temperature in figure 6.2 was not monotonic, which had the lowest point at about 400 °C. In Ref. [18] studying G92, SAXS technique was applied and found at 400 °C necking happened earlier than either lower or higher temperatures, which can be explained by the competence of strain hardening and cross section reduction. With the increase of temperature, the rate of strain hardening generally decreased, then surpassed by the rate of cross section reduction. The reason why higher temperature like 550°C and 650°C had higher fracture strain was that at high temperature strain sofening came into consideration. Lastly, the Young's modulus of these 3 Fe were found to be very simliar as expected.

6.2 Microscopic Phase Performance

Applying XRD technique when conducting tensile test, micro-structure information such as lattice strain evolution, lattice anisotropy and load partitioning phenomena have been retrieved for G91, G92 and T91. This section will discuss their similarities and differences.

Lattice strain information were calculated from diffraction peak position fitting and Bragg's Law as ex-

plained in Chapter 4. Lattice strain VS. engineering strain plots from all these 3 Fe variations showed very similar profiles. To conclude, precipitates like $M_{23}C_6$ and MX generally bear higher lattice strain than Fe matrix, but the gap would decrease with the elevation of temperature. Moreover, lattice strain yielded much later than that of Fe matrix planes, contributing to material strength after engineering yielding point.

Anisotropy effect, evidenced by the fact that different diffraction planes of Fe matrix and precipitates had different engineering stress vs lattice strian curve, causing different Young's modulus for different planes. As shown in table 4.3 and figure 4.4, 4.5 in Chapter 4; figure 4, table 2 in Ref. [19]; and figure 6, 7, table 1 in Ref. [18], the anisotropy effect of these three Fe variations are very similar to each other with minor numeric value difference.

Load partitioning effect, similar to that of lattice strain VS. engineering strain profiles, was plotted by calculated applied stress VS. lattice strain as shown in figure 4.7 in Chapter 4, figure 4 of the above G91 reference and figure 8 of G92 reference. Precipitates taking higher load than Fe matrix effect, also called load transfering effect, was more obvious at lower temperature given the large gap between Fe and precipitates in these figures. When temperature went higher, like lattice strain vs engineering strain, this load partitioning or strengthening effect was also weakened. In a word, G91, G92 and T91 shared highly similar load partitioning effect due to their similarity of composition.

6.3 Dislocation and Grain Comparison

Dislocation density and grain size are important characteristics of metal materials to interpret mechanical properties, so G91, G92 and T91 are no exceptions. Both XRD and Microscopy techniques can perform its own estimation based certain theories.

XRD technique uses W-H plot to seperate peak broadening into strain effect (dislocation) and size effect (crystalline size) due to their different diffraction angle dependence. The precision of this model is affected by many parameters, such as peak fitting error, W-H model correctness and parameters selection. On the other hand, TEM is the most widely used microscopy technique to count the dislocation density and grain size. TEM's advantage is that it directly studies samples lifted out of real bulk materials, then researchers can see what is really inside the materials. Its disadvantage, however, is that tiny specimen may not be a good representative of the bulk and sample preparation may introduce defects. Facing this fact, the common

practise is to combine results from the two techniques and compare them.

In this study of T91, both XRD and TEM were applied on the 450°C sample and they gave out pretty close dislocation density results, $1.25 \pm 0.42 \times 10^{15}\ m^{-2}$ and $1.0 \pm 0.1 \times 10^{15}\ m^{-2}$ at fracture as shown at the end of Chapter 5. In G91 reference [19], the as-received sample's dislocation density was calculated to be $1.0 \pm 0.5 \times 10^{15}\ m^{-2}$ (XRD) and $9.7 \times 10^{13}\ m^{-2}$ (TEM). For T91 dislocation figure 4.8, the starting dislocation density was about $3 \times 10^{14}\ m^{-2}$, a little bit higher due to sample preparation, but of the same magnitude with the G91 as-received results. As for the variation trend of dislocation density, in figure 8 of Ref.[19] for G91, at RT the disloatioin density (proportional to slope square) increased to yield point then plateaued; at 650°C remained stablely. Compared with 4.8, at RT dislocation density of G91 and T91 performed similarly but at 550°C T91 increased first the dropped slowly while at 650°C G91 always remained steady. The difference above need more research and evidence to validate.

As for crystalline size related information, there are also several similar but different concepts such as coherent scattering volume, coherent scattering length or dislocation cell size, thus it is reasonable to compare their general variation trend instend of their exact values. From figure 8 of Ref.[19], at RT coherent scattering volume (proportional to inverse of y-intercept) increased a little bit then decreased; at 650°C remained unchanged. For T91, figure 4.9 was interpreted as the coherent scattering length instead. At RT and 450°C, it stayed stable for a while then dropped, while at 550°C it stablized, dropped but increased after UTS. The performance differences between T91 and G91 (G92 data unavailable) at higher temperature may be traced to elemental difference, which requires more future work to explain.

Chapter 7

CONCLUSIONS AND FUTURE WORK

To sum up, this thesis concentrated on XRD data processing work to study T91 F/M steels behaviors in in-situ WAXS tensile test under RT, 450°C, and 550°C in the first four chapters, while another part of efforts were spent to microscopically analyze the post-tensile samples to validate the result of XRD in Chapter 5. Discussion and Comparison of T91 with G91 and G92 were carried out in Chapter 6. The conclusions and possible future work can be summarized in this last chapter as below.

7.1 In-situ XRD Tensile Test Conclusions

XRD experiment and data processing gave out lots of useful knowledge about the behaviours of T91 steels under tensile test, both microscopically and macroscopically. Engineering Stress-Strain curves contained UTS, YS and Young's Modulus information under 3 temperatures to compare with T91 variants. XRD diffraction peaks were then fitted and used to derive lattice spacing and strain for each existent phases with certain *(hkl)* planes. $M_{23}C_6$ and MX precipitates were found to bear higher lattice strain than Fe matrix, similar to that of load partitioning effect. This thesis found that with the elevation of experiment tempetature, second phase's high lattice and load partitioning effects were less obvious within the plastic regime. In addition, peak broadening phenomenon was carefully studied to quantify dislocation density and coherent scattering length information. It was found that dislocation density in Fe matrix ρ behaved differently within different strain regimes. Before UTS, all ρ's of three temperatures increased. After UTS, ρ stabled first then climbed for RT, plateaued for 450°C and decreased continuously for 550°C. Since W-H plot failed to give the reliable values of crystalline size, Scherrer Equation instead was used to quantify and compare the coherent scattering length L_{310} using Fe (310) plane. Before UTS, all L_{310}'s increased. After UTS, it dropped dramatically for RT, remained stable for 450°C and climbed greatly for 550°C.

The variation trend of dislocation density ρ's were in fact inverse to that of coherent scattering length L_{310}. This outcome is no surprising since every sample went through the combination effect of elevated temperature and applied tension. At low temperature such as RT, tensile tension dominated, dislocation

density was higher and coherent scattering length was smaller due to internal deformation and rupture coming from tension. Under high temperature such as 550°C, high temperature recrystallization and subgrain boundaries thermal disappearance prevailed, reducing dislocation density and raising up coherent scattering length. More complicated explanation requires void volume fraction and other parameters which can be obtained from Small Angle X-Ray Scattering (SAXS).

7.2 Electron Microscopy Conclusions

Post tensile test samples were then investigated using microscopy techniques, including SEM, EDS, OM and TEM, and reached the following conclusions. Ragged fracture cross-section of RT sample was featured by cracks and cleavages while for higher tempearture more voids and dimples dominated on relative smooth surface. These surfaces suggested more violently and faster fracture process for lower temperature tensile test. EDS mapping found non-metallic elements were enriched in fracture protrusions while metallic elements were more uniformly distributed. Mechanical polishing and chemical etching enabled the viewing of dark marthensitic plates and white ferrite under OM. Finally, FIB prepared specimen was observed with more sophisticated TEM, validating the morphology of grains, existance of precipates and dislocations. To conclude, the microscopy work agreed well with the results of XRD previously, once again, suggesting the effectiveness and reliability of XRD technique being used to infer the structure of materials.

7.3 Limitations And Future Work

Although in-situ XRD experiment and post-tensile microscopy work gave out valuable and consistent results, there are still limitations of this thesis and room to imporve.

During XRD experiment, the SAXS data were not collected, disabling the calculation of void volume and flow stress using Tayler Equation 4.5. XRD data processing proved that different *(hkl)* would gave out different coherent scattering lenght scale or even variation trend from that of L_{310}, EBSD can be applied to study the dynamic grain evolution under tensile test. Dislocation density and coherent scattering length results were not satisfying in terms of precision, thus more careful sample preparation and data processing are needed for extending work.

As for microscopy part, due to time and effort limitations, FIB-made TEM sample was limited to 450°C only, making it unable to compare the results and study temperature effects. Future work should also inclue RT and 450°C samples, and pay attention to TEM sample quality control. Another imperfection is that SEM EDS surface mapping only gave limited information about precipitates and clusters at surface. Further

work can try to apply Scanning Transmission Electron Microscopy (STEM) technique on TEM samples to study the precipitates elemental mapping inside the studied materials.

Appendix A

Peak Broadening Separation With Pseudo-Voigt Profile

During X-Ray Diffraction (XRD) experiments of studying materials, diffracted beams generally form peaks shapes distribution of detected signals. There exists several functions that can fit these peaks to find their centers and broadenings. When it comes to study the particle size and strain broadening effects, the Voigt function is the one widely used [46]. Original Voigt function is a convolution of Gaussian and Lorentzian functions [47] shown as in equation A.1 to A.3.

$$V(x;\sigma,\gamma) = \int_{-\infty}^{\infty} G(x^{'};\sigma)L(x-x^{'};\gamma)dx^{'} \tag{A.1}$$

$$G(x;\sigma) = \frac{e^{-x^2}/(2\sigma^2)}{\sigma\sqrt{2\pi}} \tag{A.2}$$

$$L(x;\gamma) = \frac{\gamma}{\pi(x^2+\gamma^2)} \tag{A.3}$$

Where x is the shift from the peak center, G represents Gaussian profile while L represents Lorentzian profile. σ and γ are the parameters for Gaussian (Normal) distribution and Lorentz (Cauchy) distribution, respectively.

On average, convolution calculation costs intensive computation price thus a good approximation was invented and called pseudo-Voigt function as equation A.4. Pseudo-Voigt is by definition a linear combination of Gaussian and Lorentzian functions, making it easy and fast to computate with safisfying precision [48].

$$V_p(2\theta) = I_0 \cdot (\eta \cdot L(2\theta) + (1-\eta) \cdot G(2\theta)) \tag{A.4}$$

Where I_0 is peak center intensity; 2θ is two times of the diffraction angle; η is Lorentzian profile fraction,

$L(2\theta)$ and $G(2\theta)$ are Lorentzian and Gaussian components, repectively.

During Matlab peaks fitting of this thesis, in order to save computation time but still maintain good precision, psdudo-Voigt profile model was used. For the purpose of post-processing, Lorentzian profile fraction η and total broadening (by FWHM) Γ were computed and recorded automatically. If η was too small (for example , less than 0.2, from experience), then the Gaussian part dominated the broadening. When η too large (take 0.8 as an example) appeared, Lorentzian part prevailed. Both of the two extreme η scenarios are easy to deal with as instrumental broadening can be easily removed by square root deduction or direct deduction with equation 3.5 or equation 3.4. The worst scenario is when η is neither close to 0 nor close to 1, which requires further data manipulation by equation A.5 and A.6 to reduce errors .

$$\Gamma = (\Gamma_G^5 + 2.69296\Gamma_G^4\Gamma_L + 2.42843\Gamma_G^3\Gamma_L^2 + 4.47163\Gamma_G^2\Gamma_L^3 + 0.07842\Gamma_G\Gamma_L^4 + \Gamma_L^5)^{\frac{1}{5}} \tag{A.5}$$

$$\eta = 1.36603(\Gamma_L/\Gamma) - 0.47719(\Gamma_L/\Gamma)^2 + 0.11116(\Gamma_L/\Gamma)^3 \tag{A.6}$$

When Γ and η are given, it is easy to compute Γ_G and Γ_L by solving the two equations with two unknown variables. After getting the true broadening by removing the instrumental broadening with equation 3.5 or equation 3.4, equation A.5 can be used to combine them back together to obtain the true broadening coming only from the test materials.

References

[1] Steven Chu and Arun Majumdar. Opportunities and challenges for a sustainable energy future. *Nature*, 488(7411):294–303, 2012.

[2] D Butler. Energy: Nuclear power's new dawn. *Nature*, 429(6989):238–240, 2004.

[3] Risto Tarjanne and Sauli Rissanen. Nuclear Power: Least-Cost Option for Baseload Electricity in Finland. *Symposium A Quarterly Journal In Modern Foreign Literatures*, (September 2000), 2010.

[4] Giorgio Locatelli, Mauro Mancini, and Nicola Todeschini. Generation IV nuclear reactors: Current status and future prospects. *Energy Policy*, 61:1503–1520, 2013.

[5] S. J. Zinkle and G. S. Was. Materials challenges in nuclear energy. *Acta Materialia*, 61(3):735–758, 2013.

[6] Todd Allen, Jeremy Busby, Mitch Meyer, and David Petti. Materials challenges for nuclear systems. *Materials Today*, 13(12):14 – 23, 2010.

[7] S A Maloy, M R James, and M.B. Toloczko. the High Temperature Tensile Properties of Ferritic-Martensitic and Austenitic Steels After Irradiation in an 800 MeV Proton Beam. pages 669–678.

[8] M. Scapin, L. Peroni, C. Fichera, and A. Cambriani. Tensile behavior of T91 steel over a wide range of temperatures and strain-rate up to 104 s-1. *Journal of Materials Engineering and Performance*, 23(8):3007–3017, 2014.

[9] Shen Jianian, Zhou Longjiang, and Li Tiefan. High-temperature oxidation of fe-cr alloys in wet oxygen. *Oxidation of Metals*, 48(3):347–356, 1997.

[10] G. Odette and B. Wirth. A computational microscopy study of nanostructural evolution in irradiated pressure vessel steels. *Journal of Nuclear Materials*, 251:157–171, 1997.

[11] Gary S. Was. *FUNDAMENTALS OF RADIATION MATERIALS SCIENCE*, volume 9783540494713. Spinger, University of Michigan, Ann Arbor, USA, 2007.

[12] C. Domain, C. S. Becquart, and L. Malerba. Simulation of radiation damage in Fe alloys: An object kinetic Monte Carlo approach. *Journal of Nuclear Materials*, 335(1):121–145, 2004.

[13] R.L. Klueh and A.T. Nelson. Ferritic/martensitic steels for next-generation reactors. *Journal of Nuclear Materials*, 371(1–3):37 – 52, 2007. Nuclear Fuels and Structural Materials 1Proceedings of the First Symposium on Nuclear Fuels and Structural Materials for Next Generation Nuclear Reactors.

[14] RL Klueh. Elevated-temperature ferritic and martensitic steels and their application to future nuclear reactors. 2004.

[15] A.P. Greeff, C.W. Louw, and H.C. Swart. The oxidation of industrial fecrmo steel. *Corrosion Science*, 42(10):1725 – 1740, 2000.

[16] Yongsun Yi, Byeonghak Lee, Sungho Kim, and Jinsung Jang. Corrosion and corrosion fatigue behaviors of 9cr steel in a supercritical water condition. *Materials Science and Engineering: A*, 429(1–2):161 – 168, 2006.

[17] R.L. Klueh, D.S. Gelles, S. Jitsukawa, A. Kimura, G.R. Odette, B. van der Schaaf, and M. Victoria. Ferritic/martensitic steels – overview of recent results. *Journal of Nuclear Materials*, 307–311, Part 1:455 – 465, 2002.

[18] Leyun Wang, Meimei Li, and Jonathan Almer. In situ characterization of grade 92 steel during tensile deformation using concurrent high energy x-ray diffraction and small angle x-ray scattering. *Journal of Nuclear Materials*, 440(1–3):81 – 90, 2013.

[19] Leyun Wang, Meimei Li, and Jonathan Almer. Investigation of deformation and microstructural evolution in grade 91 ferritic–martensitic steel by in situ high-energy x-rays. *Acta Materialia*, 62:239 – 249, 2014.

[20] Yinbin Miao, Kun Mo, Zhangjian Zhou, Xiang Liu, Kuan Che Lan, Guangming Zhang, Michael K. Miller, Kathy A. Powers, Jonathan Almer, and James F. Stubbins. In situ synchrotron tensile investigations on the phase responses within an oxide dispersion-strengthened (ODS) 304 steel. *Materials Science and Engineering A*, 625:146–152, 2015.

[21] Yinbin Miao, Kun Mo, Zhangjian Zhou, Xiang Liu, Kuan-Che Lan, Guangming Zhang, Michael K. Miller, Kathy A. Powers, Zhi-Gang Mei, Jun-Sang Park, Jonathan Almer, and James F. Stubbins. On the microstructure and strengthening mechanism in oxide dispersion-strengthened 316 steel: A coordinated electron microscopy, atom probe tomography and in situ synchrotron tensile investigation. *Materials Science and Engineering: A*, 639:585 – 596, 2015.

[22] Kun Mo, Zhangjian Zhou, Yinbin Miao, Di Yun, Hsiao Ming Tung, Guangming Zhang, Weiying Chen, Jonathan Almer, and James F. Stubbins. Synchrotron study on load partitioning between ferrite/martensite and nanoparticles of a 9Cr ODS steel. *Journal of Nuclear Materials*, 455(1-3):376–381, 2014.

[23] Kun Mo, Hsiao-Ming Tung, Jonathon Almer, Meimei Li, Xiang Chen, Weiying Chen, Jon B. Hansen, and James F. Stubbins. Synchrotron Radiation Study on Alloy 617 and Alloy 230 for VHTR Application. *Journal of Pressure Vessel Technology*, 135(2):021502, 2013.

[24] A. Khorsand Zak, W.H. Abd. Majid, M.E. Abrishami, and Ramin Yousefi. X-ray analysis of zno nanoparticles by williamson–hall and size–strain plot methods. *Solid State Sciences*, 13(1):251 – 256, 2011.

[25] Xiang Liu, Kun Mo, Yinbin Miao, Kuan-Che Lan, Guangming Zhang, Wei-Ying Chen, Carolyn Tomchik, Rachel Seibert, Jeff Terry, and James F. Stubbins. Investigation of thermal aging effects on the tensile properties of Alloy 617 by in-situ synchrotron wide-angle X-ray scattering. *Materials Science and Engineering: A*, 651:55–62, 2016.

[26] Guangming Zhang, Zhangjian Zhou, Kun Mo, Yinbin Miao, Xiang Liu, Jonathan Almer, and James F. Stubbins. The evolution of internal stress and dislocation during tensile deformation in a 9Cr ferritic/martensitic (F/M) ODS steel investigated by high-energy X-rays. *Journal of Nuclear Materials*, 467:50–57, 2015.

[27] Loveleen K. Brar, Gourav Singla, and O. P. Pandey. Evolution of structural and thermal properties of carbon-coated tac nanopowder synthesized by single step reduction of ta-ethoxide. *RSC Adv.*, 5:1406–1416, 2015.

[28] C. Keller, M. M. Margulies, Z. Hadjem-Hamouche, and I. Guillot. Influence of the temperature on the tensile behaviour of a modified 9Cr-1Mo T91 martensitic steel. *Materials Science and Engineering A*, 527(24-25):6758–6764, 2010.

[29] M. Ashrafi-Nik. Thermo hydraulic optimisation of the eurisol ds target. Issue 2, 2006.

[30] Vincent Gaffard. *Experimental study and modelling of high temperature creep flow and damage behaviour of 9Cr1Mo-NbV steel weldments*. PhD thesis, Grenoble Institute of Technology, France, 2004.

[31] B. Clausen, T. Lorentzen, and T. Leffers. Self-consistent modelling of the plastic deformation of f.c.c. polycrystals and its implications for diffraction measurements of internal stresses. *Acta Materialia*, 46(9):3087 – 3098, 1998.

[32] M.A. Weisser, A.D. Evans, S. Van Petegem, S.R. Holdsworth, and H. Van Swygenhoven. In situ room temperature tensile deformation of a 1steel using synchrotron and neutron diffraction. *Acta Materialia*, 59(11):4448 – 4457, 2011.

[33] M.L. Young, J.D. Almer, M.R. Daymond, D.R. Haeffner, and D.C. Dunand. Load partitioning between ferrite and cementite during elasto-plastic deformation of an ultrahigh-carbon steel. *Acta Materialia*, 55(6):1999 – 2011, 2007.

[34] W.F. Hosford. *Mechanical Behavior of Materials*. Cambridge University Press, 2010.

[35] T. Ungár and A. Borbély. The effect of dislocation contrast on xray line broadening: A new approach to line profile analysis. *Applied Physics Letters*, 69(21):3173–3175, 1996.

[36] Á. Révész, T. Ungár, A. Borbély, and J. Lendvai. Dislocations and grain size in ball-milled iron powder. *Nanostructured Materials*, 7(7):779–788, 1996.

[37] S. Morito, J. Nishikawa, and T. Maki. Dislocation density within lath martensite in fe-c and fe-ni alloys. *ISIJ International*, 43(9):1475–1477, 2003.

[38] M. Matijasevic, E. Lucon, and A. Almazouzi. Behavior of ferritic/martensitic steels after n-irradiation at 200 and 300 °c. *Journal of Nuclear Materials*, 377(1):101 – 108, 2008. Spallation Materials TechnologyProceedings of the Eighth International Workshop on Spallation Materials Technology.

[39] K Ramakanth. *Basics of X-ray Diffraction and its Application*. I.K. International I.K. Publishing House Pvt. Ltd, New Dehli, 2007.

[40] Leroy Alexander and Harold P. Klug. Determination of crystallite size with the xray spectrometer. *Journal of Applied Physics*, 21(2):137–142, 1950.

[41] David C Joy. *Scanning electron microscopy*. Wiley Online Library, 2006.

[42] P.J. Ennis, A. Zielinska-Lipiec, O. Wachter, and A. Czyrska-Filemonowicz. Microstructural stability and creep rupture strength of the martensitic steel {P92} for advanced power plant. *Acta Materialia*, 45(12):4901 – 4907, 1997.

[43] Elliott Fray. The heat treatment and microstructural optimization of a t91 / fe12cr2si steel composite for use as piping and fuel cladding in the lead-bismuth cooled nuclear reactor. 2012.

[44] Rutash Mittal, Lucky Goyal, and Buta Singh Sidhu. Study of Corrosion Behavior of SA213T91 Boiler Steel in the Environment of Air and Molten Salt of Na 2 SO 4 - 60 %. *Ijrmet*, 5762:58–63, 2013.

[45] David B. Williams and C. Barry Carter. *Transmission Electron Microscopy*. Springer US, New York, 2 edition, 2009.

[46] R. a. Young and D. B. Wiles. Profile shape functions in Rietveld refinements. *Journal of Applied Crystallography*, 15(4):430–438, 1982.

[47] Ivan Kupka. The voigt profile as a sum of a gaussian and a lorentzian functions, when the weight coefficient depends only on the widths ratio. 1(1):4–6, 2002.

[48] P Thompson, D E Cox, and J B Hastings. Rietveld refinement of debye-scherrer synchrotron x-ray data from al2o3. *Journal of Applied Crystallography*, 20(2):79–83, 1987.